



Study of $D_{s1}(2460)^+ \rightarrow D_s^+ \pi^+ \pi^-$ in $B \rightarrow \bar{D}^{(*)} D_s^+ \pi^+ \pi^-$ decays

LHCb collaboration[†]

Abstract

An amplitude analysis of the $D_{s1}(2460)^+ \rightarrow D_s^+ \pi^+ \pi^-$ transition is performed simultaneously in $B^0 \rightarrow D^- D_s^+ \pi^+ \pi^-$, $B^+ \rightarrow \bar{D}^0 D_s^+ \pi^+ \pi^-$, and $B^0 \rightarrow D^{*-} D_s^+ \pi^+ \pi^-$ decays. The study is based on a data sample of proton-proton collisions recorded with the LHCb detector at centre-of-mass energies of $\sqrt{s} = 7, 8,$ and 13 TeV, corresponding to a total integrated luminosity of 9 fb^{-1} . A clear double-peak structure is observed in the $m(\pi^+ \pi^-)$ spectrum of the $D_{s1}(2460)^+ \rightarrow D_s^+ \pi^+ \pi^-$ decay. The data can be described either with a model including $f_0(500)$, $f_0(980)$ and $f_2(1270)$ resonances, in which the contributions of $f_0(980)$ and $f_2(1270)$ are unexpectedly large, or with a model including $f_0(500)$, a doubly charged open-charm tetraquark state $T_{c\bar{s}}^{++}$ and its isospin partner $T_{c\bar{s}}^0$. If the former is considered implausible, the $T_{c\bar{s}}$ states are observed with high significance, and the data are consistent with isospin symmetry. When imposing isospin constraints between the two $T_{c\bar{s}}$ states, their mass and width are determined to be $2327 \pm 13 \pm 13 \text{ MeV}$ and $96 \pm 16 \text{ }^{+170}_{-23} \text{ MeV}$, respectively, where the first uncertainty is statistical and the second is systematic. The mass is slightly below the DK threshold, and a spin-parity of 0^+ is favoured with high significance.

Submitted to Science Bulletin

© 2024 CERN for the benefit of the LHCb collaboration. [CC BY 4.0 licence](#).[†]Authors are listed at the end of this paper.

1 Introduction

Since the observation of the $D_{s_0}^*(2317)^+$ and $D_{s_1}(2460)^+$ mesons in 2003 [1, 2], their nature has been discussed extensively but without a firm conclusion [3–12]. The $D_{s_0}^*(2317)^+$ and $D_{s_1}(2460)^+$ masses are much lower than the expectation in the quark model [13–15]. The observed degeneracy between the masses of the charmed mesons ($D_0^*(2300)^{0(\pm)}$ and $D_1(2430)^0$) and the charmed-strange mesons ($D_{s_0}^*(2317)^\pm$ and $D_{s_1}(2460)^\pm$) in the $(0^+, 1^+)$ doublet [16], indicates that the $D_{s_0}^*(2317)^+$ and $D_{s_1}(2460)^+$ states probably have nontrivial internal structure.¹ Due to their relatively small masses, their decays to D^*K states are forbidden, resulting in total widths of a few MeV or less [17] and substantial branching fractions for the isospin-violating decays to $D_s^{(*)+}\pi^0$ final states.² The isospin-conserving decay, $D_{s_1}(2460)^+ \rightarrow D_s^+\pi^+\pi^-$, also occurs at a sizeable rate [17, 18]. Theoretical calculations predict a double-bump lineshape in the $\pi^+\pi^-$ invariant-mass spectrum in this decay if the $D_{s_1}(2460)^+$ meson is a D^*K hadronic molecule [19].

The LHCb collaboration recently reported the observation of two neutral tetraquark states, labelled $T_{cs_0}(2900)^0$ and $T_{cs_1}(2900)^0$, in $B^- \rightarrow D^+D^-K^-$ decays [20, 21].³ Later, LHCb also observed a doubly charged tetraquark and its neutral partner, labelled $T_{c\bar{s}}(2900)^{++}$ and $T_{c\bar{s}}(2900)^0$ with $I(J^P) = 1(0^+)$ where I denotes the isospin of the particle, in $B \rightarrow \bar{D}D_s^+\pi$ decays [22, 23]. The proximity of the masses of these states to the $D^*\bar{K}^*$ threshold suggests that they might be $D^*\bar{K}^*$ bound states [24–26]. Furthermore, recent theoretical work suggests that the multiplet including $T_{c\bar{s}}(2900)^{++}$, $T_{c\bar{s}}(2900)^0$, and $T_{cs_0}(2900)^0$ tetraquarks could be the radial excitation of a lighter multiplet containing the $D_{s_0}^*(2317)$ state [27]. If so, scalar DK bound states with isospin 1 near the DK threshold are also expected and the relationship between this triplet and the $D_{s_0}^*(2317)^+$ state needs further clarification [28]. This motivates the study of three-body $D_{s_1}(2460)^+$ decays to investigate the potential existence of $D_s\pi$ structures that may couple to the DK channel. Such research could shed new light on the internal structures of the $D_{s_0}^*(2317)^+$ and $D_{s_1}(2460)^+$ mesons.

In this paper, the results from a combined amplitude analysis of the $D_{s_1}(2460)^+ \rightarrow D_s^+\pi^+\pi^-$ transition in $B^0 \rightarrow D^-D_s^+\pi^+\pi^-$, $B^+ \rightarrow \bar{D}^0D_s^+\pi^+\pi^-$, and $B^0 \rightarrow D^{*-}D_s^+\pi^+\pi^-$ decays are presented. The study is based on a data sample of proton-proton (pp) collisions recorded with the LHCb detector at centre-of-mass energies of $\sqrt{s} = 7, 8, \text{ and } 13 \text{ TeV}$, corresponding to a total integrated luminosity of 9 fb^{-1} . The use of fully reconstructed B -meson decays allows kinematic constraints on the decay chain to be applied, which improves the resolution, suppresses background contributions and enables the determination of the quantum numbers that affect the decay amplitudes.

2 Detector and simulation

The LHCb detector [29, 30] is a single-arm forward spectrometer covering the pseudorapidity range $2 < \eta < 5$, designed for the study of particles containing b or c quarks. The detector includes a high-precision tracking system consisting of a silicon-strip vertex detector surrounding the pp interaction region, a large-area silicon-strip

¹The form J^P denotes the total spin J and parity P .

²Natural units in which $c = \hbar = 1$ are used throughout the article.

³The inclusion of charge-conjugate processes is implied throughout the article.

detector located upstream of a dipole magnet with a bending power of about 4 T m, and three stations of silicon-strip detectors and straw drift tubes placed downstream of the magnet. The tracking system provides a measurement of the momentum, p , of charged particles with a relative uncertainty that varies from 0.5% at low momentum to 1.0% at 200 GeV. The minimum distance of a track to a primary pp collision vertex (PV), the impact parameter (IP), is measured with a resolution of $(15 + 29/p_T) \mu\text{m}$, where p_T is the component of the momentum transverse to the beam, in GeV. Different types of charged hadrons are distinguished using information from two ring-imaging Cherenkov detectors.

In this analysis, the online selections include hardware and software triggers. The hardware trigger criteria are satisfied by energy deposits in the calorimeter associated with the signal candidate decay. The software trigger requires a two-, three- or four-track secondary vertex with significant displacement from any primary pp interaction vertex. In general, at least one charged particle must have a transverse momentum $p_T > 1.6$ GeV and be inconsistent with originating from a PV.

Simulation is required to determine the detector efficiency (which includes the detector acceptance and selection requirements). In the simulation, pp collisions are generated using PYTHIA [31] with a specific LHCb configuration [32]. Decays of unstable particles are described by EVTGEN [33], in which final-state radiation is generated using PHOTOS [34]. The interaction of the generated particles with the detector, and its response, are implemented using the GEANT4 toolkit [35] as described in Ref. [36]. The underlying pp interaction is reused multiple times using REDECAY [37], with an independently generated signal decay for each interaction.

3 Selection

The intermediate $D_{s1}(2460)^+$, D^{*-} , D_s^+ , \bar{D}^0 , and D^- mesons are reconstructed through the following decays: $D_{s1}(2460)^+ \rightarrow D_s^+ \pi^+ \pi^-$, $D^{*-} \rightarrow \bar{D}^0 \pi^-$, $D_s^+ \rightarrow K^- K^+ \pi^+$, $\bar{D}^0 \rightarrow K^+ \pi^-$, and $D^- \rightarrow K^+ \pi^- \pi^-$. The charged K and π candidates are formed from well-reconstructed tracks that are inconsistent with originating from any PV, with particle identification information consistent with the corresponding mass hypothesis. The D_s^+ , \bar{D}^0 , and D^- candidates are required to have good vertex quality and significant displacement with respect to all PVs. Combinatorial background is suppressed with requirements on the outputs of trained Boosted Decision Tree (BDT) classifiers [38–40], which take as input transverse momentum, tracking, vertexing and particle identification variables. Each BDT classifier is trained with simulated D mesons from B decays as signal and combinatorial background from mass sideband regions in data. The mass of the reconstructed candidates must be within ± 30 MeV of the corresponding known mass.⁴ The $D_{s1}(2460)^+$ and D^{*-} candidates are formed from combinations of charged pions with D_s^+ and \bar{D}^0 candidates, respectively, where the combined vertices must be of good quality and displaced from all PVs. The mass difference between the D^{*-} candidate and its \bar{D}^0 decay product is required to be less than 150 MeV. The reconstructed $D_{s1}(2460)^+$ candidate mass must be less than 2700 MeV for the fit to the $m(D_s^+ \pi^+ \pi^-)$ invariant-mass distribution used to determine the signal and background yields, and must be within ± 10 MeV of its known value for the subsequent amplitude fit.

⁴Unless otherwise specified, known values of particle properties are taken from Ref. [16].

The B candidates are formed by combining a $\bar{D}^{(*)}$ and a $D_{s1}(2460)^+$ candidate, and requiring a well-reconstructed vertex which is displaced from all PVs. The momentum vector of each B candidate is required to point back to the PV where it is hypothesised to have been produced, referred to hereafter as the associated PV. The reconstructed B -meson mass is required to be within ± 40 MeV of its known value. For the $B^+ \rightarrow \bar{D}^0 D_{s1}(2460)^+$ signal channel, an additional requirement that the $\bar{D}^0 \pi^-$ invariant-mass be larger than 2020 MeV is applied to veto potential D^{*-} background contamination. After applying the selection criteria, around 5% of the remaining events contain more than one B candidate; in these cases only one is kept randomly.

Kinematic fits [41] are used at different stages of the data analysis. By default, the B candidate is constrained to have originated from the associated PV. When considering the B -candidate mass distribution, further constraints on the masses of the $\bar{D}^{(*)}$ and D_s^+ candidates to their known values are applied. For the invariant-mass fit described in the next section, in addition to the above constraints, the B -candidate mass is fixed in the kinematic fit to its known value to improve the $D_{s1}(2460)^+$ mass resolution. Finally, an additional $D_{s1}(2460)^+$ mass constraint is applied in the fit used to obtain the four-momenta of the final-state particles for the amplitude analysis. This is valid since the small $D_{s1}(2460)^+$ width [17] has negligible impact on the analysis.

4 Invariant-mass fit

The $m(D_s^+ \pi^+ \pi^-)$ invariant-mass spectra for the three signal channels after all selection criteria are shown in Fig. 1. Clear $D_{s1}(2460)^+$ signals are observed in all three channels, together with a smoothly varying combinatorial background and a small contribution from $D_{s1}(2536)^+ \rightarrow D_s^+ \pi^+ \pi^-$ decays. Extended unbinned maximum-likelihood fits to the data, where the lower bound is the kinematic threshold $m_{D_s^+} + 2m_{\pi^+}$, are performed to extract signal and background yields for the subsequent amplitude fit. The $D_{s1}(2460)^+$ and $D_{s1}(2536)^+$ components are modelled by relativistic Breit–Wigner functions [16] convolved with a common Gaussian function to account for experimental resolution. The $D_{s1}(2460)^+$ Breit–Wigner mass and width are free to vary in the fit while the $D_{s1}(2536)^+$ parameters are fixed to their known values. The width of the Gaussian resolution function is shared between the $D_{s1}(2460)^+$ and $D_{s1}(2536)^+$ components and is allowed to vary in the fit. The combinatorial background is modelled by an ARGUS function [42] with fixed kinematic threshold of 2247 MeV and the shape parameter governing the slope is free to vary in the fit.

The fit results for the three signal channels are shown together with the data distributions in Fig. 1. The signal and background yields inside the signal region, defined to be ± 10 MeV around the $D_{s1}(2460)^+$ known mass, are summarised in Table 1. In total around 800 signal events are obtained.

5 Amplitude analysis formalism

The amplitudes of the signal decays are expressed using the helicity formalism with an isobar approach [43–45], where the total amplitude is a coherent sum of quasi-two-body amplitudes. The Blatt–Weisskopf factor in the amplitudes is fixed to 3.0 GeV^{-1} in the amplitude fit. Each resonant lineshape is modelled by a relativistic Breit–Wigner (RBW)

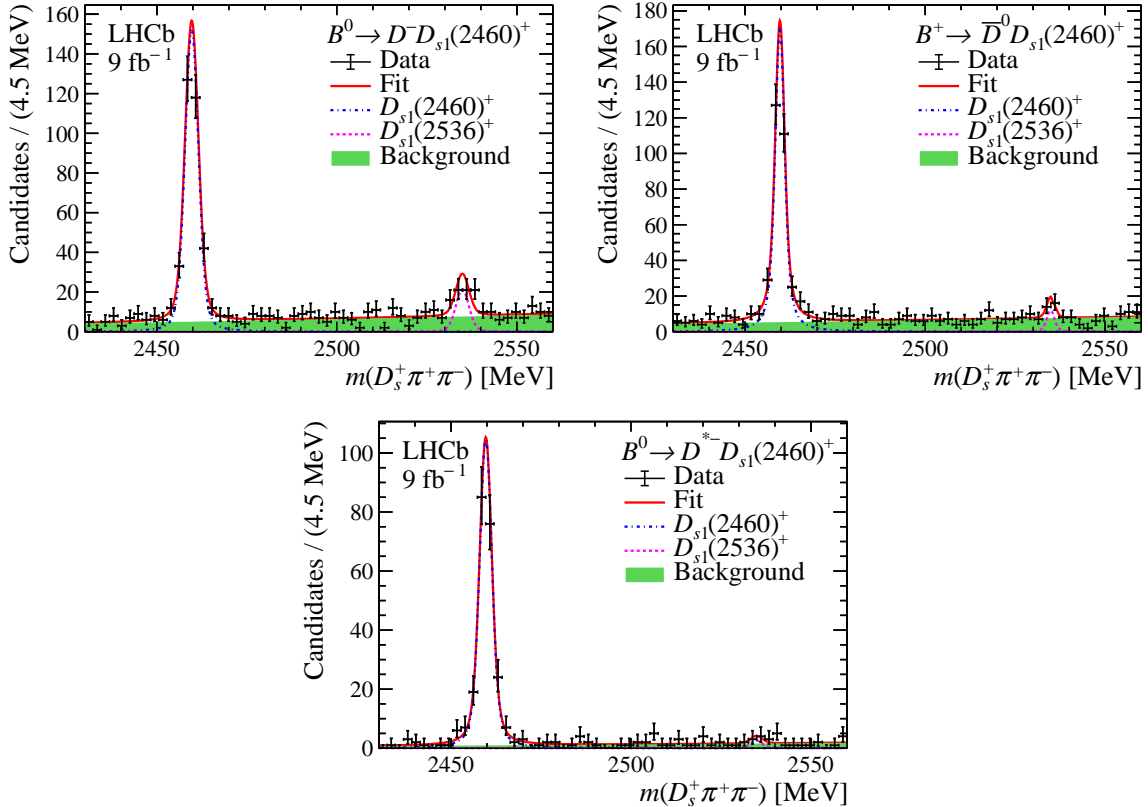


Figure 1: Invariant-mass distributions for the $D_{s1}(2460)^+$ candidates in the three signal channels (black points) shown with the fit model (solid lines). The coloured region shows the combinatorial background.

Table 1: Estimated signal and background yields inside the $D_{s1}(2460)^+$ mass window, together with the signal fraction. Note that the extrapolation of the background yield into the signal window allows uncertainties on the yields (N) to be smaller than \sqrt{N} .

Channel	Signal yield	Background yield	Signal fraction (%)
$B^0 \rightarrow D^- D_s^+ \pi^+ \pi^-$	305 ± 20	22 ± 1	93.2 ± 0.4
$B^+ \rightarrow \bar{D}^0 D_s^+ \pi^+ \pi^-$	279 ± 18	24 ± 1	92.2 ± 0.5
$B^0 \rightarrow D^{*-} D_s^+ \pi^+ \pi^-$	205 ± 14	4 ± 1	98.0 ± 0.2

function, if not specified otherwise. The $f_0(980)$ state is modelled by a modified Flatté function [46, 47], with its parameters fixed according to Refs. [47, 48]. The K-matrix model suggested in Ref. [49, 50] is used as an alternative $\pi\pi$ S-wave lineshape. Due to the small phase space available in $D_{s1}(2460)^+ \rightarrow D_s^+ \pi^+ \pi^-$ decays, the accessible $m(\pi\pi)$ range is limited and the analysis has little sensitivity to some parameters of this model; such parameters are fixed to zero in the fit.

An alternative model for $\pi\pi$ lineshapes, based on the assumption of the $D_{s1}(2460)^+$ meson being a compact or a molecular state [19] and hereafter referred to as the chiral dynamics model, is also tested. This model includes separate compact and molecular components, each obtained using a two-dimensional interpolation method, with relative fractions set by a parameter that is determined in the fit.

Another K-matrix model based on the scattering length approximation, considering DK and $D_s\pi$ coupled-channel effects, is used as a possible lineshape to describe $T_{c\bar{s}}$ states. Details of this model can be found in the review of resonances in Ref. [16] and also in Ref. [51]. The scattering K-matrix is parameterised as

$$K = \begin{pmatrix} \gamma & \beta \\ \beta & \gamma_2 \end{pmatrix}, \quad (1)$$

where γ is proportional to the scattering length in the elastic DK channel, β describes the coupling to the inelastic $D_s\pi$ channel, and γ_2 includes the possible interaction in the $D_s\pi$ channel. The lineshape for the $D_s\pi$ decay is

$$f^{\text{K-matrix}} = \frac{\beta^2 \rho_{DK} + i\gamma_2(i\gamma\rho_{DK} - 1)}{\beta^2 \rho_{DK}\rho_{D_s\pi} + (i\gamma\rho_{DK} - 1)(i\gamma_2\rho_{D_s\pi} - 1)}, \quad (2)$$

and the scattering length is

$$a = \frac{1}{8\pi\sqrt{s_{\text{thr}}}} (\gamma + i\beta^2\rho_{D_s\pi}(s_{\text{thr}})), \quad (3)$$

where $s_{\text{thr}} = (m_D + m_K)^2$, and $\rho_{DK/D_s\pi}$ denotes the dimensionless phase-space term. The parameter γ_2 is fixed to zero in the amplitude fit, since there is little sensitivity to it in the channels under study.

An unbinned maximum-likelihood fit is performed simultaneously to the three signal channels. The negative log-likelihood function for each channel is defined as

$$-\ln \mathcal{L} = - \sum_{i \in \text{data}} \ln [f_{\text{sig}} \mathcal{P}_{\text{sig}}(\xi_i; \Lambda) + (1 - f_{\text{sig}}) \mathcal{P}_{\text{bkg}}(\xi_i; \Lambda)], \quad (4)$$

where f_{sig} denotes the signal fraction in the signal region, determined from the $m(D_s^+\pi^+\pi^-)$ fit described previously. The term \mathcal{P}_{sig} stands for the signal probability density function (PDF) for candidate i at position ξ_i in phase space,

$$\mathcal{P}_{\text{sig}}(\xi_i; \Lambda) = \frac{|A(\xi_i; \Lambda)|^2}{\int |A(\xi; \Lambda)|^2 \varepsilon(\xi) d\xi}, \quad (5)$$

where Λ denotes the set of parameters to be determined in the fit to data. Here, A is the total amplitude and $\varepsilon(\xi)$ denotes the efficiency variation over the phase space, which is determined from simulated samples after applying simulation corrections on the tracking and trigger efficiencies, obtained using control samples [52, 53]. The masses and widths of the considered resonances and their coupling constants are shared between the three channels. The background PDF $\mathcal{P}_{\text{bkg}}(\xi_i; \Lambda)$ is estimated using events in the $m(D_s^+\pi^+\pi^-)$ sidebands [2247, 2440] MeV and [2560, 2660] MeV, and is described with a kernel density function [54].

The results of the amplitude analysis are expressed in terms of fit fractions. The fit fraction F_i for resonance i is calculated based on the fitted values of the parameters $\hat{\Lambda}$, and is defined as

$$F_i = \frac{\int |A_i(\xi; \hat{\Lambda})|^2 d\xi}{\int |\sum_k A_k(\xi; \hat{\Lambda})|^2 d\xi}, \quad (6)$$

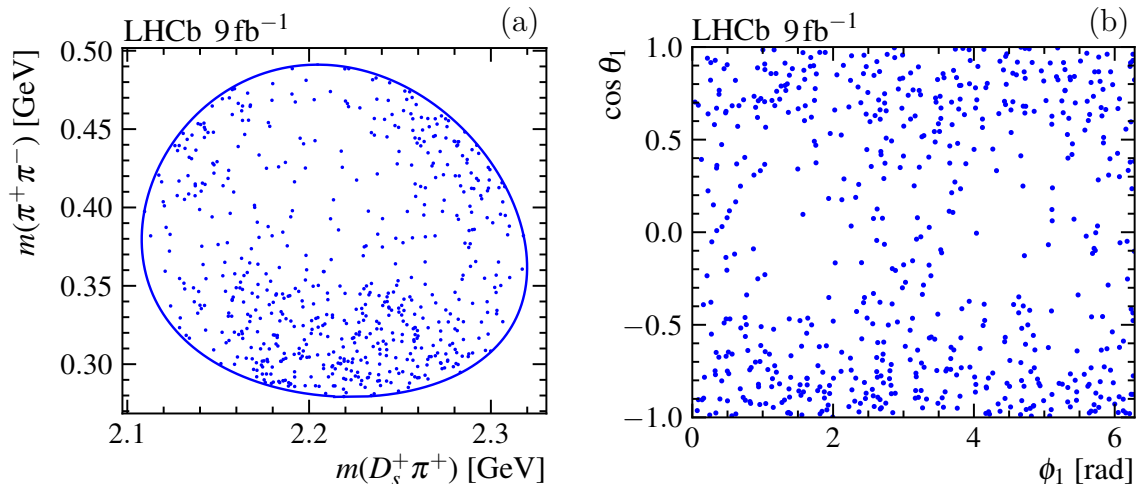


Figure 2: Distributions of selected candidates in the (a) $m(D_s^+\pi^+) - m(\pi^+\pi^-)$ plane and (b) $\phi_1 - \cos\theta_1$ plane, combining the $B^0 \rightarrow D^- D_{s1}(2460)^+$ and $B^+ \rightarrow \bar{D}^0 D_{s1}(2460)^+$ channels. The blue solid line on the left plot denotes the boundary of the $D_{s1}(2460)^+ \rightarrow D_s^+ \pi^+ \pi^-$ Dalitz plot. Background contributions are not subtracted and no efficiency corrections are applied.

where $A_i(\xi)$ is the contribution to the amplitude from resonance i . The interference between any two components i and j , F_{ij} , is quantified as

$$F_{ij} = \frac{\int 2 \Re \left\{ A_i A_j^*(\xi; \hat{\Lambda}) \right\} d\xi}{\int |\sum_k A_k(\xi; \hat{\Lambda})|^2 d\xi}. \quad (7)$$

6 Amplitude fit

Figure 2 shows the distributions of selected candidates in the $m(D_s^+\pi^+) - m(\pi^+\pi^-)$ and $\phi_1 - \cos\theta_1$ planes, combining the $B^0 \rightarrow D^- D_{s1}(2460)^+$ and $B^+ \rightarrow \bar{D}^0 D_{s1}(2460)^+$ channels. These four variables fully describe the dynamics of the two included decays, while in the $B^0 \rightarrow D^{*-} D_{s1}(2460)^+$ case two additional angles related to D^{*-} decays are necessary, making it inappropriate to combine the three distributions. Here, θ_1 is the helicity angle of the $R(\pi\pi)$ resonance in $D_{s1}(2460)^+ \rightarrow D_s^+ R(\pi\pi)$ decays and ϕ_1 is the angle between the decay planes of $D_{s1}(2460)^+ \rightarrow D_s^+ R(\pi\pi)$ and $R(\pi\pi) \rightarrow \pi^+\pi^-$ decays. Full definitions are shown in Fig. 7 in the supplemental material. The data cluster in three phase-space regions, two of which are highlighted as a double bump in the $m(D_s^+\pi^+)$ distribution when requiring $m(\pi^+\pi^+) > 0.39$ GeV. The corresponding distributions for $B^0 \rightarrow D^{*-} D_{s1}(2460)^+$ decays and projections on the efficiency-corrected $m(\pi^+\pi^-)$, $m(D_s^+\pi^+)$, $\cos\theta_1$ and ϕ_1 distributions for the three channels are shown in the supplemental material.

In the $D_{s1}(2460)^+ \rightarrow D_s^+ \pi^+ \pi^-$ decays, conventional quark-antiquark resonances are only possible in the $\pi\pi$ channel. Therefore, models with only $\pi\pi$ resonances are attempted first.

A summary of the relative negative log likelihoods (ΔNLLs) for different models is given in Table 2. When considering only $\pi\pi$ resonance contributions, two models give the best description of the data without adding nonsignificant resonant contributions. One contains the $f_0(500)$, $f_0(980)$ and $f_2(1270)$ states, and the other describes the $\pi\pi$

Table 2: Relative negative log likelihoods (ΔNLL) and numbers of fit parameters for all tested models. The ΔNLL value is calculated with the model $f_0(500) + \text{K-matrix } T_{c\bar{s}}(0^+)$ as reference. Smaller values of ΔNLL correspond to better fits.

Model	ΔNLL	Number of fit parameters
Chiral dynamics	252.4	5
K-matrix $\pi\pi$ S-wave	249.0	6
$f_0(500) + f_0(980)$	245.2	8
$f_0(500) + f_0(980) + \rho(770)^0$	148.0	12
$f_0(500) + f_0(980) + f_2(1270)$	3.7	12
$f_0(500) + f_0(980) + f_2(1270) + \rho(770)^0$	-2.8	16
K-matrix $\pi\pi$ S-wave + $f_2(1270)$	5.9	10
$f_0(500) + \text{RBW } T_{c\bar{s}}(0^+)$	3.5	10
$f_0(500) + \text{K-matrix } T_{c\bar{s}}(0^+)$	0.0	10
$f_0(500) + f_0(980) + \text{RBW } T_{c\bar{s}}(0^+)$	-3.0	12
$f_0(500) + \rho(770)^0 + \text{RBW } T_{c\bar{s}}(0^+)$	-1.1	14
$f_0(500) + f_2(1270) + \text{RBW } T_{c\bar{s}}(0^+)$	-4.3	14
$f_0(500) + \text{RBW } T_{c\bar{s}}(1^-)$	62.9	12

Table 3: Summary of fit results for different models described in detail. Values quoted without uncertainties are taken from previous measurements [16, 48] and are fixed in the fits. The two sources of uncertainty are statistical and systematic. For the models containing $T_{c\bar{s}}$ states the quoted fit fraction is the value for each of the isospin partners, and the quoted $T_{c\bar{s}}$ mass and width parameters are the pole mass and width.

Model	Resonance	Mass [MeV]	Width [MeV]	Fractions [%]
$f_0(500) + f_0(980) + f_2(1270)$	$f_0(500)$	$376 \pm 9 \pm 16$	$175 \pm 23 \pm 16$	$197 \pm 35 \pm 23$
	$f_0(980)$	945.5	167	$187 \pm 38 \pm 43$
	$f_2(1270)$	1275.4	186.6	$29 \pm 2 \pm 1$
$f_0(500) + \text{RBW } T_{c\bar{s}}(0^+)$	$f_0(500)$	$464 \pm 23 \pm 14$	$214 \pm 28 \pm 8$	$199^{+42}_{-47} \pm 39$
	$T_{c\bar{s}}^{++}/T_{c\bar{s}}^0$	$2312 \pm 27 \pm 11$	$264 \pm 46 \pm 21$	$126^{+27}_{-17} \pm 20$
$f_0(500) + \text{K-matrix } T_{c\bar{s}}(0^+)$	$f_0(500)$	$474 \pm 30 \pm 18$	$224 \pm 23 \pm 16$	$248^{+40}_{-54} \pm 39$
	$T_{c\bar{s}}^{++}/T_{c\bar{s}}^0$	$2327 \pm 13 \pm 13$	$96 \pm 16 \pm 23$	$156^{+27}_{-38} \pm 25$

S-wave with a K-matrix component and includes an additional $f_2(1270)$ resonance. The projections onto $m(\pi^+\pi^-)$, $m(D_s^+\pi^+)$ and $m(D_s^+\pi^+)$ requiring $m(\pi^+\pi^-) > 0.39 \text{ GeV}$ for the first model are shown in Fig. 3. The corresponding $m(\pi^+\pi^-) - m(D_s^+\pi^+)$ and $\phi_1 - \cos\theta_1$ distributions are shown in Fig. 11 in the supplemental material. The inclusion of the $f_2(1270)$ component is necessary to obtain good agreement with the data. The fits with models excluding this component have much higher ΔNLL values, as seen in Table 2. The inclusion of a $\rho(770)^0$ component leads to a small improvement in ΔNLL , but this is insignificant bearing in mind the change in the number of free parameters of the fit.

Although these models give reasonable descriptions of the data across the

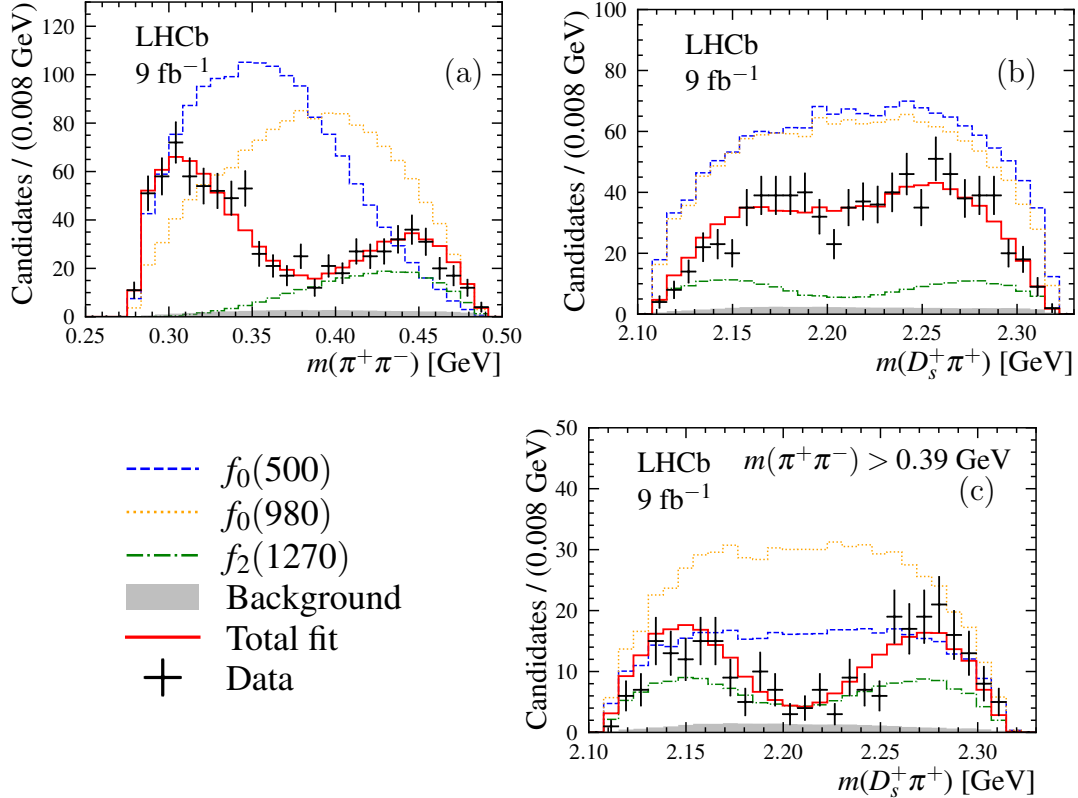


Figure 3: Comparison between data (black error bars) and results of the fit with the $f_0(500) + f_0(980) + f_2(1270)$ model (red solid line). The distributions are for the three channels combined in (a) $m(\pi^+\pi^-)$, (b) $m(D_s^+\pi^+)$, and (c) $m(D_s^+\pi^+)$ requiring $m(\pi^+\pi^-) > 0.39$ GeV. Individual components, corresponding to the background contribution estimated from $m(D_s^+\pi^+\pi^-)$ sideband regions (gray-filled) and the different resonant contributions (coloured dashed lines), are also shown as indicated in the legend.

$D_{s1}(2460)^+ \rightarrow D_s^+\pi^+\pi^-$ phase space, there are several reasons to doubt their credibility as physical descriptions of the decay amplitude. First, there is a large contribution from the $f_2(1270)$ resonance, despite the fact that the kinematic upper limit of $m(\pi^+\pi^-)$ is around $m_{f_2(1270)} - 4 \cdot \Gamma_{f_2(1270)}$, where $m_{f_2(1270)}$ and $\Gamma_{f_2(1270)}$ are the known $f_2(1270)$ mass and width. Such a large contribution from the tail of a lineshape is barely plausible. A similar argument applies to the $f_0(980)$ contribution. Secondly, the model including both $f_0(500)$ and $f_0(980)$ components requires large destructive interference to generate the observed $m(\pi^+\pi^-)$ structures, with the total fit fraction summing to $(413 \pm 66)\%$. This destructive interference between different components of the $\pi\pi$ S-wave is also present in the K-matrix description. While large interference effects are inevitable in an amplitude analysis with broad components overlapping in a small phase space, the dramatic effects seen here are markedly different from what is seen in $\pi\pi$ S-waves in other processes [48, 55–61]. Furthermore, as shown in Table 3, the fitted value of the $f_0(500)$ mass, and to a lesser extent also that of its width, are different from what is seen in other processes [16].

In addition to the results shown above, some fits with the $f_0(500)$, $f_0(980)$ and $f_2(1270)$ states converge to another solution with a similar ΔNLL value. This solution, however, has a very large interference between the $f_0(500)$ and $f_0(980)$ resonances leading to unstable results. This solution also finds the $f_0(500)$ mass to be even smaller (around 190 MeV)

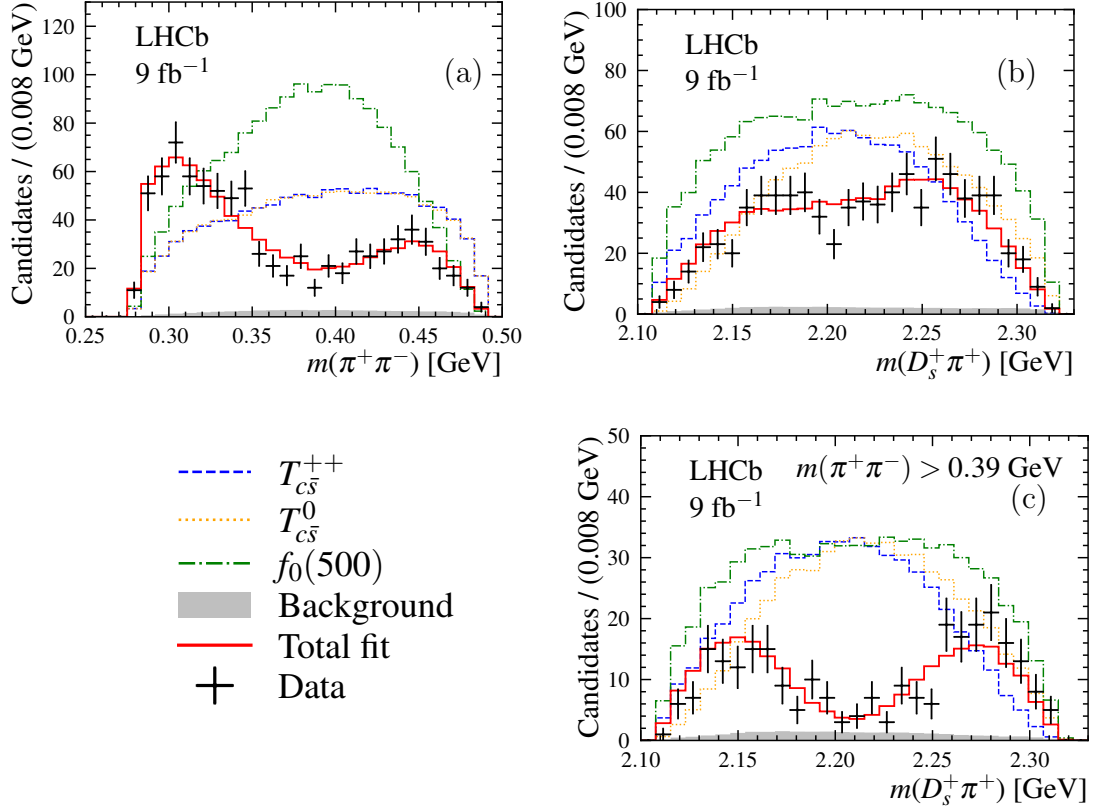


Figure 4: Comparison between data (black error bars) and results of the fit with the $f_0(500) +$ RBW $T_{c\bar{s}}(0^+)$ model. The distributions are for the three channels combined in (a) $m(\pi^+\pi^-)$, (b) $m(D_s^+\pi^+)$, and (c) $m(D_s^+\pi^+)$ requiring $m(\pi^+\pi^-) > 0.39$ GeV. Individual components, corresponding to the background contribution estimated from $m(D_s^+\pi^+\pi^-)$ sideband regions (gray-filled) and the different resonant contributions (coloured dashed lines), are also shown as indicated in the legend.

and the $f_0(500)$ width larger than 700 MeV. It is not discussed further.

Due to these unsatisfactory aspects of the fit results for models containing only $\pi^+\pi^-$ resonances, models with additional exotic states decaying to $D_s^+\pi^\pm$, referred to as $T_{c\bar{s}}^{++}$ and $T_{c\bar{s}}^0$ states, are considered. In all cases, both the $T_{c\bar{s}}^{++}$ and $T_{c\bar{s}}^0$ isospin partners are included, and by default their coupling constants, masses and widths (or parameters β and γ for the K-matrix model) are constrained to be the same following isospin symmetry.

As seen in Table 2, models with only $f_0(500)$ and $T_{c\bar{s}}$ states with spin-parity $J^P = 0^+$ give approximately as good descriptions of the data as the best (but, as discussed above, arguably implausible) models without $T_{c\bar{s}}$ states. Two possible $T_{c\bar{s}}$ lineshapes, RBW and K-matrix, are considered and give similar fit quality. The projections of the fit results are given in Figs. 4 and 5. The corresponding plots in the $m^2(\pi^+\pi^-) - m^2(D_s^+\pi^+)$ and $\phi_1 - \cos(\theta_1)$ planes with the RBW model are shown in Fig. 12 in the supplemental material. A second solution with similar ΔNLL is also obtained, but is quite unstable and therefore is not discussed further.

As seen from the large fit fractions in Table 3, fits with these models have similarly large destructive interference effects as in models without the $T_{c\bar{s}}$ states. It may also be noted that the fitted $f_0(500)$ mass and width values are now in better agreement with previous measurements [16]. The mass of the $T_{c\bar{s}}$ states is comparable between the RBW

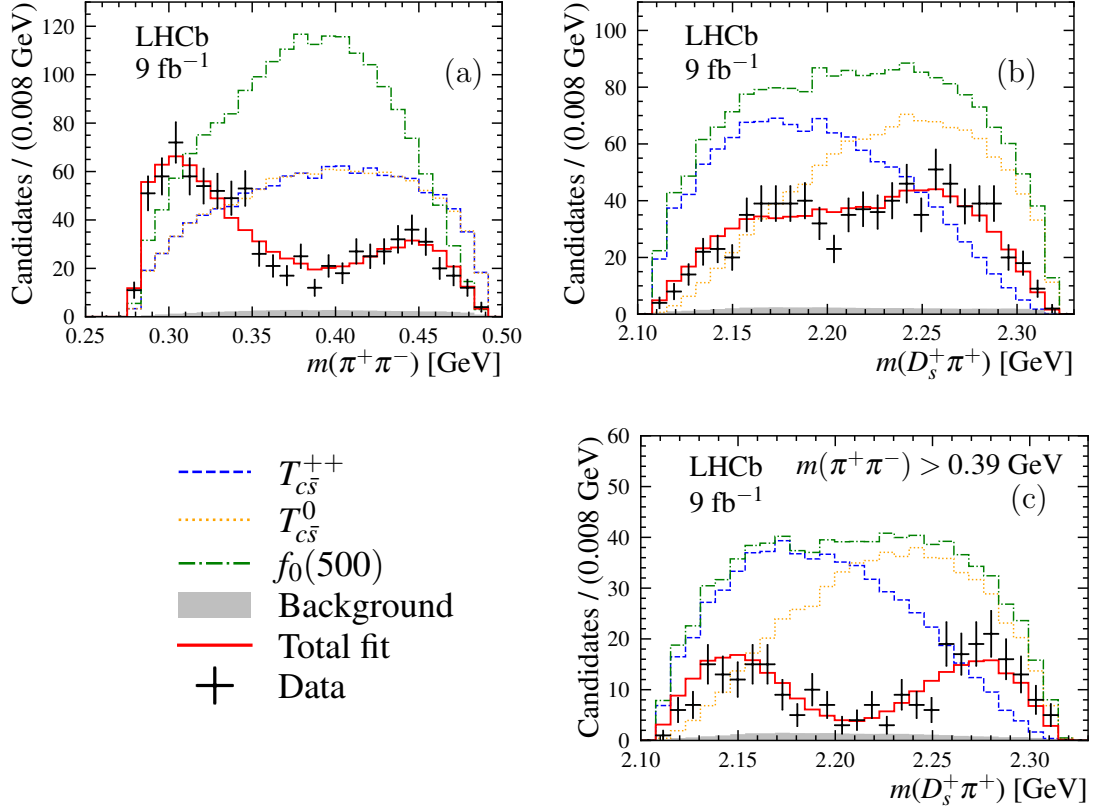


Figure 5: Comparison between data (black error bars) and results of the fit with the $f_0(500)$ + K-matrix $T_{c\bar{s}}(0^+)$ model (red solid line). The distributions are for the three channels combined in (a) $m(\pi^+\pi^-)$, (b) $m(D_s^+\pi^+)$, and (c) $m(D_s^+\pi^+)$ requiring $m(\pi^+\pi^-) > 0.39$ GeV. Individual components, corresponding to the background contribution estimated from $m(D_s^+\pi^+\pi^-)$ sideband regions (gray-filled) and the different resonant contributions (coloured dashed lines), are also shown as indicated in the legend.

and K-matrix models but a large variation in the width is found. For the K-matrix model, the γ_2 parameter in Eq. (1) is fixed to 0 as it is expected that the coupling to the $D_s\pi$ channel is weak. Values of $\beta = 153 \pm 12$ and $\gamma = -259 \pm 21$ are obtained, from which the scattering length is calculated to be $-0.86(\pm 0.07) + 0.44(\pm 0.07)i$ fm, incompatible with the value predicted in Ref. [62]. The mass and width of the K-matrix model given in Table 3 are calculated in the second Riemann sheet and are also different from those predicted in Ref. [63]. When allowed to vary freely in the fit, $\gamma_2 = 47 \pm 41$ is obtained, consistent with the expectation of zero, while $\beta = 133 \pm 16$ and $\gamma = -244 \pm 17$ are consistent with the values obtained when γ_2 is fixed to 0. The Argand diagrams [16] for the RBW and K-matrix descriptions of the $T_{c\bar{s}}$ lineshape are shown in Fig. 6, and are seen to be consistent with each other.

In order to test the assumption of isospin symmetry, the coupling constants, masses, and widths of the two $T_{c\bar{s}}$ states are allowed to differ. This is done in both the RBW and K-matrix $T_{c\bar{s}}$ models, with results consistent with isospin symmetry in both cases. For example, with the K-matrix $T_{c\bar{s}}$ lineshape, the mass and width for $T_{c\bar{s}}^{++}$ ($T_{c\bar{s}}^0$) are measured to be 2325 ± 11 MeV (2325 ± 10 MeV) and 81 ± 14 MeV (118 ± 20 MeV), respectively.

Models with additional $\rho(770)^0$, $f_0(980)$ and $f_2(1270)$ components are also tested. None of these extra contributions are found to be significant. An upper limit on the fit

fraction of the isospin-breaking $D_{s1}(2460)^+ \rightarrow D_s^+ \rho(770)^0$ decay is set at 2.8% at the 90% confidence level. This is less restrictive than the upper limit of 1.7% at the 90% confidence level obtained if the model does not include any $T_{c\bar{s}}$ component. Bearing in mind the large contributions from the $f_0(980)$ and $f_2(1270)$ components in the $f_0(500) + f_0(980) + f_2(1270)$ model, it is interesting to note that the corresponding contributions are small and not significant in the $f_0(500) + f_0(980) + T_{c\bar{s}}$ and $f_0(500) + f_0(1270) + T_{c\bar{s}}$ models. An attempt is made to fit with the $\pi\pi$ resonances described by the chiral dynamics model together with $T_{c\bar{s}}$ states, but the fit results have unphysically large interference and are not further discussed.

To estimate the significance of the two $T_{c\bar{s}}$ contributions, samples of pseudodata are generated based on the results of the fit with a model containing $f_0(500)$ and $f_0(980)$ resonances only. These pseudoexperiments are each fitted both with and without $T_{c\bar{s}}$ states. The distribution of the $2\Delta\text{NLL}$ values between the two fit results is fitted with a χ^2 distribution, and the number of degrees of freedom (N_{dof}) is determined to be 6.77 ± 0.25 . Given that the $2\Delta\text{NLL}$ value from data is 490.4, the significance is estimated to be much larger than 10 standard deviations (σ). The $2\Delta\text{NLL}$ distribution is given in the supplemental material. This significance value implicitly rejects the $f_0(500) + f_0(980) + f_2(1270)$ model. If the null hypothesis is based on that model, the $T_{c\bar{s}}$ components are not significant.

The spin-parity of the $T_{c\bar{s}}$ states used in the fits is changed to 1^- instead of 0^+ . This reduces significantly the interference effects, but results in a ΔNLL value about 60 units larger than that obtained with $J^P = 0^+$ $T_{c\bar{s}}$ states. Pseudoexperiments are generated according to the fit results under this alternative spin-parity assumption to evaluate the significance of this outcome. The pseudoexperiments are fitted with both spin-0 and spin-1

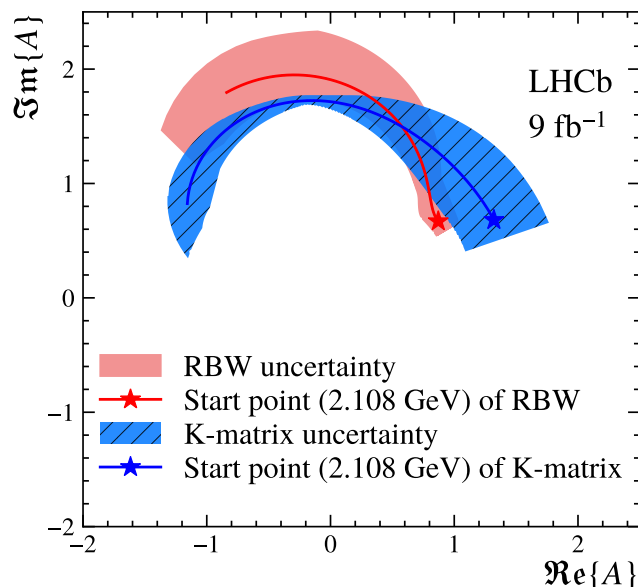


Figure 6: Argand diagrams for the variation with mass of the $T_{c\bar{s}}$ states amplitude with both RBW and K-matrix models. The red and blue stars denote the lower $m(D_s\pi)$ kinematic limit (denoted “start point”). The statistical uncertainties for the RBW and K-matrix models are marked as red solid and blue slashed bands, respectively.

models, and the distribution of $2\Delta\text{NLL}$ values is obtained. Comparing to the $2\Delta\text{NLL}$ value observed in data, the spin-parity 0^+ is favoured with 10σ significance. The $2\Delta\text{NLL}$ distribution is shown in Fig. 14 in the supplemental material.

7 Systematic uncertainties

Systematic uncertainties are evaluated on the masses, widths and fit fractions of each of the components included in the $f_0(500) + f_0(980) + f_2(1270)$, $f_0(500) + \text{RBW } T_{c\bar{s}}(0^+)$ and $f_0(500) + \text{K-matrix } T_{c\bar{s}}(0^+)$ models. The sources of systematic uncertainty are divided into five categories: the signal fraction, the background model, the efficiency map, the fixed parameters in the amplitude fit, and the choices for the lineshape models. Among them, the dominant systematic uncertainties are from the fixed parameters in the amplitude fit and the choices for lineshape models. The total systematic uncertainties presented in Table 3 are determined by combining all contributions in quadrature, and do not include the uncertainty from the choices for the $T_{c\bar{s}}$ lineshape models, which is treated later.

Most of the systematic uncertainties are estimated by performing several times the fit to data, each time varying the input parameters within their respective uncertainties, such as altering distributions or fixed parameters. The root mean squares of the distributions of the fit results are taken as the corresponding measures of systematic uncertainty. A further source of uncertainty related to the signal fraction is estimated by changing the signal shape in the $m(D_s^+\pi^+\pi^-)$ fit to a Gaussian function and calculating the resulting signal fraction. The difference between the results in the amplitude fits using the two signal fraction estimations is assigned as an additional uncertainty. The background model uncertainty is estimated by changing the background description using a different nonparameterised method to model the two-body invariant masses and helicity angles considering correlations between them. The variation in the fit results is considered as the systematic uncertainty. The efficiency map category accounts for uncertainties related to the size of the simulation sample used to describe the efficiency variation over the phase space, as well as uncertainties due to simulation corrections. The fixed parameters in the amplitude models include the Blatt–Weisskopf radius parameter and the $f_0(980)$ and $f_2(1270)$ masses and widths. The former is varied from its default value of 3.0 GeV^{-1} to 1.5 GeV^{-1} and 4.5 GeV^{-1} . The latter are varied within the uncertainties of previous measurements [16, 48]. Additionally, the effect of allowing the γ_2 parameter of the K-matrix $T_{c\bar{s}}$ model to vary in the fit is assigned as a systematic uncertainty.

Possible biases in the fit procedure are studied with pseudoexperiments generated from the fit results, and then fitted with the same model. The pull distribution for each fit parameter is modelled using a Gaussian function for symmetric distributions or a double-sided Crystal Ball function [64] for asymmetric ones. Almost all pull distributions show deviations from normal distributions that are smaller than 3σ . Nonetheless, adjustments are applied to the central values and uncertainties to correct for any potential biases and under- or over-coverage.

For the final results on the mass and width of the $T_{c\bar{s}}$ states, an additional systematic uncertainty is assigned to account for the description of the $T_{c\bar{s}}$ lineshape. The results with the $f_0(500) + \text{K-matrix } T_{c\bar{s}}(0^+)$ model are taken as the central values, and an additional asymmetric systematic uncertainty calculated as the difference in the results between the $f_0(500) + \text{RBW } T_{c\bar{s}}(0^+)$ and $f_0(500) + \text{K-matrix } T_{c\bar{s}}(0^+)$ models is assigned. This is

the dominant uncertainty on the $T_{c\bar{s}}$ width. The results for the $T_{c\bar{s}}$ mass and width are $2327 \pm 13 \pm 13 \text{ MeV}$ and $96 \pm 16_{-23}^{+170} \text{ MeV}$, respectively.

8 Summary

An amplitude analysis to study the structure of $D_{s1}(2460)^+ \rightarrow D_s^+ \pi^+ \pi^-$ decays is performed for the first time. The analysis is based on exclusively reconstructed $B^0 \rightarrow D^- D_{s1}(2460)^+$, $B^+ \rightarrow \bar{D}^0 D_{s1}(2460)^+$ and $B^0 \rightarrow D^{*-} D_{s1}(2460)^+$ decays obtained from a pp collision sample recorded at centre-of-mass energies of $\sqrt{s} = 7, 8$ and 13 TeV , corresponding to 9 fb^{-1} of integrated luminosity.

A clear double-peak structure is observed in the $m(\pi^+ \pi^-)$ spectrum of $D_{s1}(2460)^+ \rightarrow D_s^+ \pi^+ \pi^-$ decays. The data can be described well with a model including only $\pi\pi$ resonances and without $D_s^+ \pi$ exotic states, but only with implausibly large $f_0(980)$ and $f_2(1270)$ contributions. An alternative model with a new exotic $T_{c\bar{s}}^{++}$ state and its isospin partner $T_{c\bar{s}}^0$ is introduced. The $T_{c\bar{s}}$ mass and width are determined to be $2327 \pm 13 \pm 13 \text{ MeV}$ and $96 \pm 16_{-23}^{+170} \text{ MeV}$, where the first uncertainties are statistical and the second are systematic. The significance of the new states exceeds 10σ , evaluated relative to a model containing $f_0(500)$ and $f_0(980)$ contributions only, and the $T_{c\bar{s}}$ spin-parity is found to be $J^P = 0^+$ with a significance of 10σ . The $T_{c\bar{s}}$ states can be interpreted as two members of the isotriplet predicted in Ref. [27], with the masses consistent with their prediction. These results complement those obtained on other T_{cs} and $T_{c\bar{s}}$ hadrons [20–23], and are an important step to probe the nature of the $D_{s1}(2460)^+$ and $D_{s0}^*(2317)^+$ resonances.

Acknowledgements

We acknowledge important input from Alex Bondar, which helped to shape the analysis reported here. We express our gratitude to our colleagues in the CERN accelerator departments for the excellent performance of the LHC. We thank the technical and administrative staff at the LHCb institutes. We acknowledge support from CERN and from the national agencies: CAPES, CNPq, FAPERJ and FINEP (Brazil); MOST and NSFC (China); CNRS/IN2P3 (France); BMBF, DFG and MPG (Germany); INFN (Italy); NWO (Netherlands); MNiSW and NCN (Poland); MCID/IFA (Romania); MICIU and AEI (Spain); SNSF and SER (Switzerland); NASU (Ukraine); STFC (United Kingdom); DOE NP and NSF (USA). We acknowledge the computing resources that are provided by CERN, IN2P3 (France), KIT and DESY (Germany), INFN (Italy), SURF (Netherlands), PIC (Spain), GridPP (United Kingdom), CSCS (Switzerland), IFIN-HH (Romania), CBPF (Brazil), and Polish WLCG (Poland). We are indebted to the communities behind the multiple open-source software packages on which we depend. Individual groups or members have received support from ARC and ARDC (Australia); Key Research Program of Frontier Sciences of CAS, CAS PIFI, CAS CCEPP, Fundamental Research Funds for the Central Universities, and Sci. & Tech. Program of Guangzhou (China); Minciencias (Colombia); EPLANET, Marie Skłodowska-Curie Actions, ERC and NextGenerationEU (European Union); A*MIDEX, ANR, IPhU and Labex P2IO, and Région Auvergne-Rhône-Alpes (France); AvH Foundation (Germany); ICSC (Italy); Severo Ochoa and María de Maeztu Units of Excellence, GVA, XuntaGal, GENCAT, InTalent-Inditex and Prog.

Atracción Talento CM (Spain); SRC (Sweden); the Leverhulme Trust, the Royal Society and UKRI (United Kingdom).

Appendix: Supplemental material

A Definition of angles

Using the decay $B^0 \rightarrow D^{*-} D_{s1}(2460)^+$ as an example and naming the intermediate dipion resonance $R(\pi\pi)$, there are four decays accounted for in the amplitude: $B^0 \rightarrow D^{*-} D_{s1}(2460)^+$, $D^{*-} \rightarrow \bar{D}^0 \pi^-$, $D_{s1}(2460)^+ \rightarrow D_s^+ R(\pi\pi)$, and $R(\pi\pi) \rightarrow \pi^+ \pi^-$. Figure 7 shows the definitions of the helicity angles and the angles between two decay planes used to describe the amplitude. The helicity angle of the $B \rightarrow D^* D_{s1}(2460)^+$ decay is denoted as θ . The angle between the $D_{s1}(2460)^+ \rightarrow D_s^+ R(\pi\pi)$ and $D^* \rightarrow D\pi$ decay planes is denoted as $\phi_0 = \phi'_0 + \phi''_0$. The helicity angles of the $D^* \rightarrow D\pi$ and $D_{s1}(2460)^+ \rightarrow D_s^+ R(\pi\pi)$ decays are denoted as θ_0 and θ_1 , respectively. The angle between the $D_{s1}(2460)^+ \rightarrow D_s^+ R(\pi\pi)$ and $R(\pi\pi) \rightarrow \pi^+ \pi^-$ decay planes is denoted as ϕ_1 , and the helicity angle of the $R(\pi\pi) \rightarrow \pi^+ \pi^-$ decay is denoted as θ_2 .

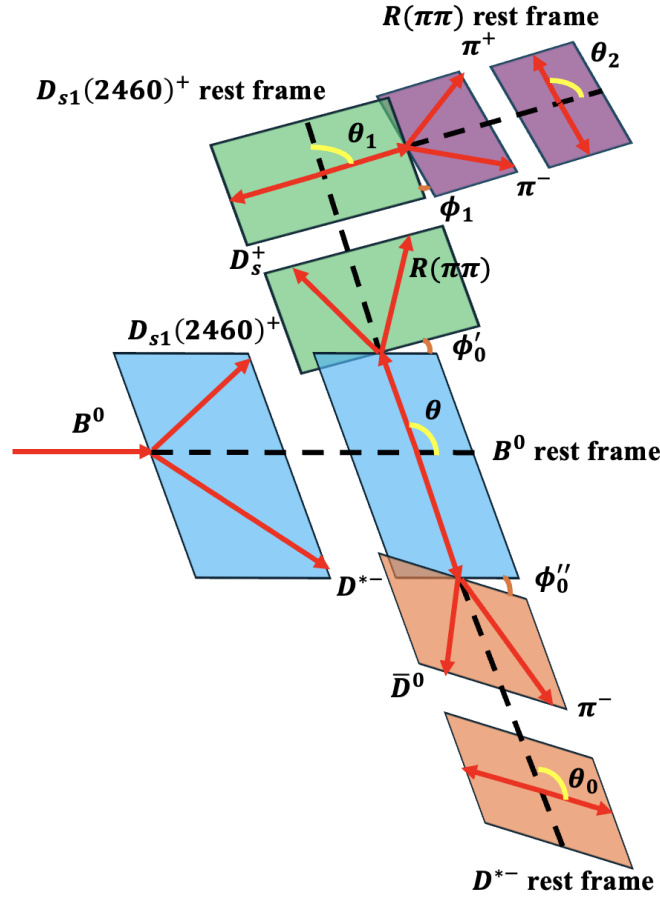


Figure 7: Definitions of the helicity angles for $B^0 \rightarrow D^{*-} D_{s1}(2460)^+$ decays, with the intermediate resonance R decaying into $\pi\pi$.

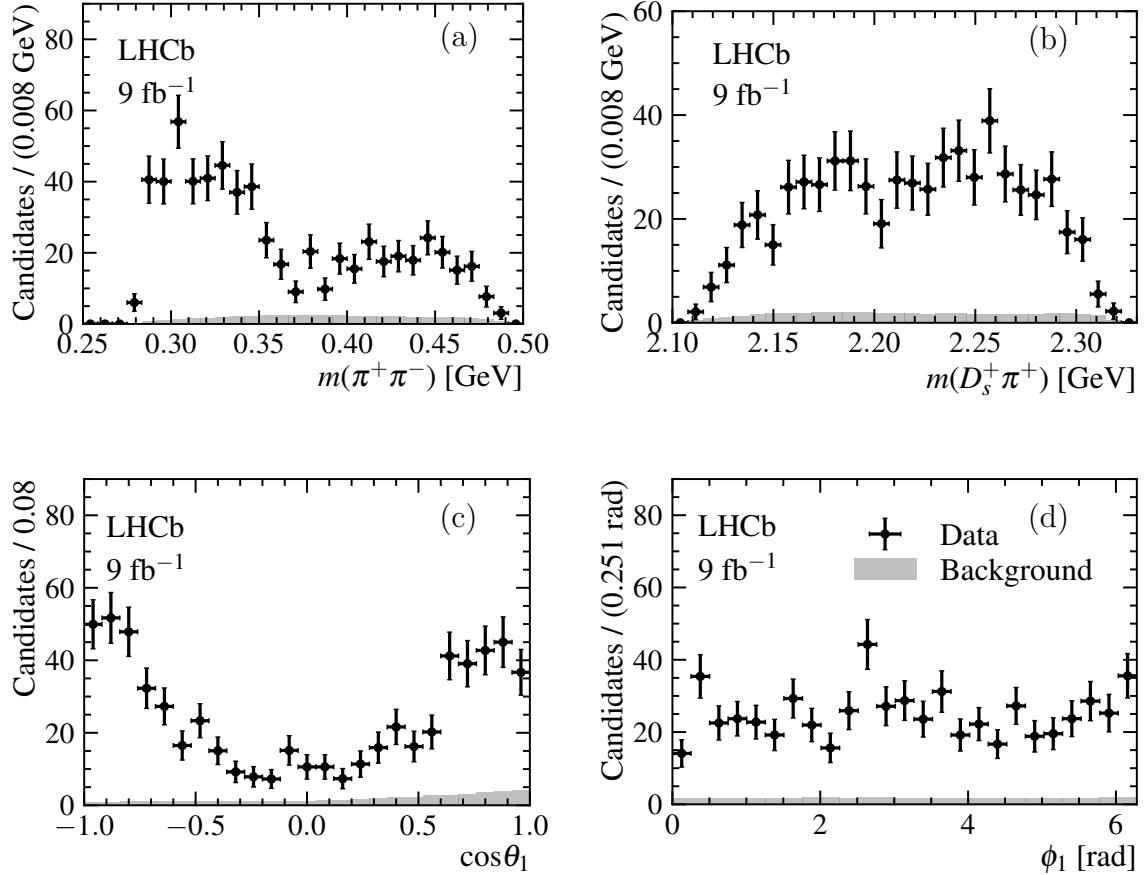


Figure 8: Efficiency-corrected distributions of the $D_{s1}(2460)^+ \rightarrow D_s^+ \pi^+ \pi^-$ phase-space variables including (a) $m(\pi^+ \pi^-)$, (b) $m(D_s^+ \pi^+)$, (c) $\cos \theta_1$ and (d) ϕ_1 combining the $B^0 \rightarrow D^- D_{s1}(2460)^+$ and $B^+ \rightarrow \bar{D}^0 D_{s1}(2460)^+$ channels, where black dots with error bars denote data points and gray histograms denote background.

B Data distributions

The efficiency-corrected data distributions combining $B^0 \rightarrow D^- D_{s1}(2460)^+$ and $B^+ \rightarrow \bar{D}^0 D_{s1}(2460)^+$ channels are shown in Fig. 8. The corresponding distributions for the $B^0 \rightarrow D^{*-} D_{s1}(2460)^+$ channel are shown in Fig. 9, while two-dimensional distributions for this channel are shown in Fig. 10.

C Pull distributions

The distributions in the $m^2(\pi^+ \pi^-) - m^2(D_s^+ \pi^+)$ and $\phi_1 - \cos(\theta_1)$ planes, superimposed on the normalised residual between adaptive binned data and model (pull) for the $f_0(500) + f_0(980) + f_2(1270)$ model and the $f_0(500) + \text{RBW } T_{c\bar{s}}^{++}$ model, are shown in Figs. 11 and 12, respectively. The adaptive binning is chosen such that each bin contains enough data points, so the χ^2 value can be correctly evaluated.

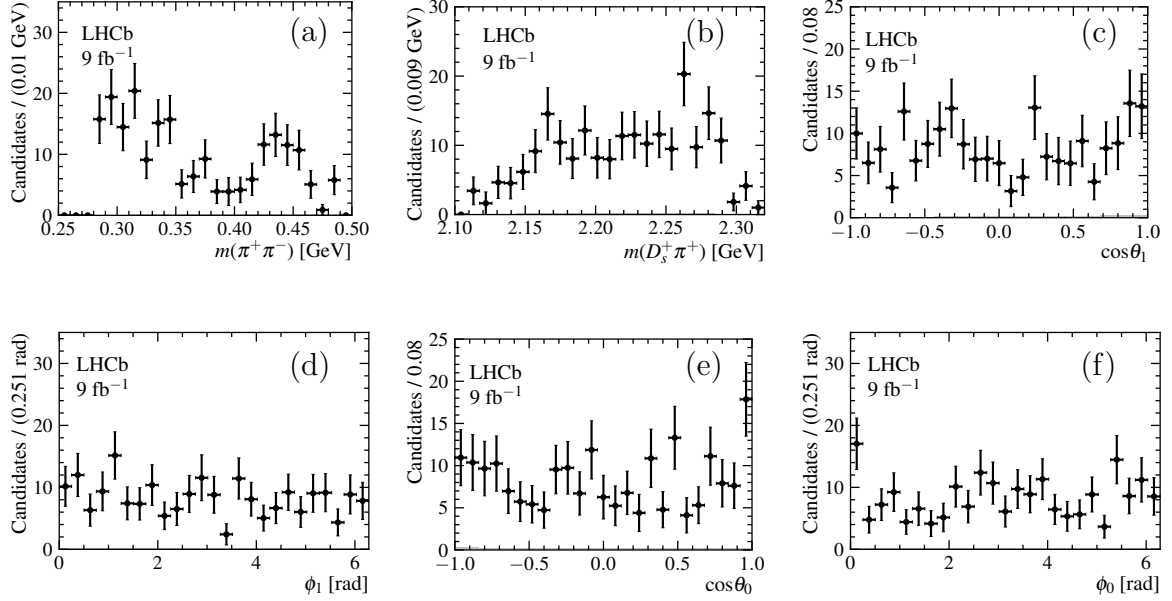


Figure 9: Efficiency-corrected distributions of the $D_{s1}(2460)^+ \rightarrow D_s^+ \pi^+ \pi^-$ phase-space variables including (a) $m(\pi^+ \pi^-)$, (b) $m(D_s^+ \pi^+)$, (c) $\cos \theta_1$, (d) ϕ_1 , (e) $\cos \theta_0$ and (f) ϕ_0 for the $B^0 \rightarrow D^{*-} D_{s1}(2460)^+$ channel, where black dots with error bars denote data points and the background is not shown due to its low contribution.

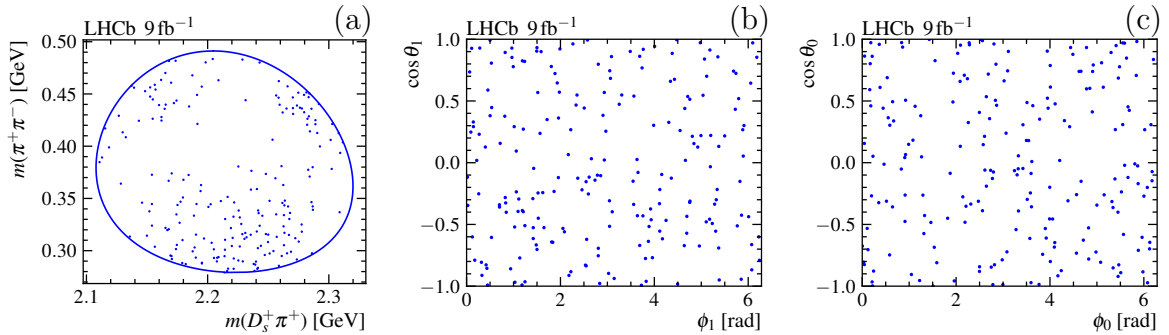


Figure 10: Distributions of selected candidates in the (a) $m(D_s^+ \pi^+) - m(\pi^+ \pi^-)$ plane, (b) $\phi_1 - \cos \theta_1$ plane and (c) $\phi_0 - \cos \theta_0$ plane for the $B^0 \rightarrow D^{*-} D_{s1}(2460)^+$ channel.

D Significance test

The $2\Delta\text{NLL}$ distribution obtained from pseudoexperiments is shown in Fig. 13, and is fitted with a χ^2 distribution. Given that the $2\Delta\text{NLL}$ value from data is 490.4, the significance of two $T_{c\bar{s}}$ contributions is estimated to be much larger than 10σ .

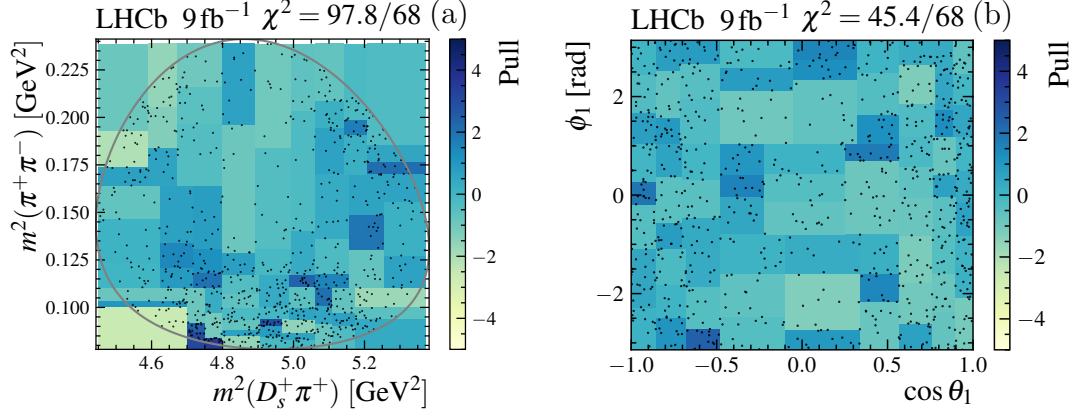


Figure 11: Data distributions in the (a) $m^2(\pi^+\pi^-) - m^2(D_s^+\pi^+)$ and (b) $\phi_1 - \cos(\theta_1)$ planes combining the three signal channels, superimposed on the normalised residuals between adaptive binned data and model (pull) for the $f_0(500) + f_0(980) + f_2(1270)$ model. The gray solid line in (a) denotes the boundary of the $D_{s1}(2460)^+ \rightarrow D_s^+\pi^+\pi^-$ Dalitz plot.

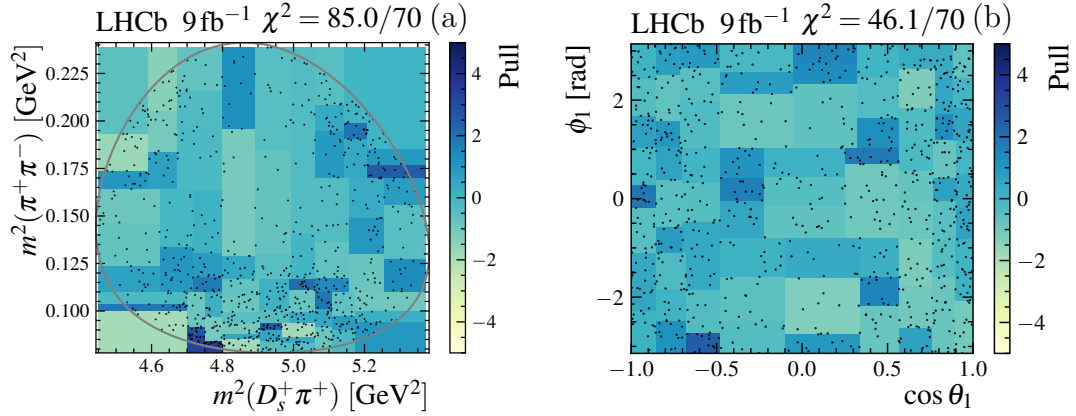


Figure 12: Data distributions in the (a) $m^2(\pi^+\pi^-) - m^2(D_s^+\pi^+)$ and (b) $\phi_1 - \cos(\theta_1)$ planes combining the three signal channels, superimposed on the normalised residuals between adaptive binned data and model (pull) for the $f_0(500) + \text{RBW } T_{c\bar{s}}^{++}$ model. The gray solid line in (a) denotes the boundary of the $D_{s1}(2460)^+ \rightarrow D_s^+\pi^+\pi^-$ Dalitz plot.

E Spin-parity test

The $2\Delta\text{NLL}$ distributions obtained from pseudoexperiments are shown in Fig. 14. The blue histogram denotes the distribution obtained from an ensemble of pseudoexperiments generated according to the results of the fit to data with the spin-0 hypothesis, which has a mean consistent with the $2\Delta\text{NLL}$ value observed in data (violet line). The red histogram denotes the distribution obtained from a corresponding ensemble with the spin-1 hypothesis, and is fitted with a Gaussian function, the result of which is shown (green line). The difference between the $2\Delta\text{NLL}$ value observed in data and the mean value of the spin-1 pseudoexperiments corresponds to a significance of 10σ , demonstrating

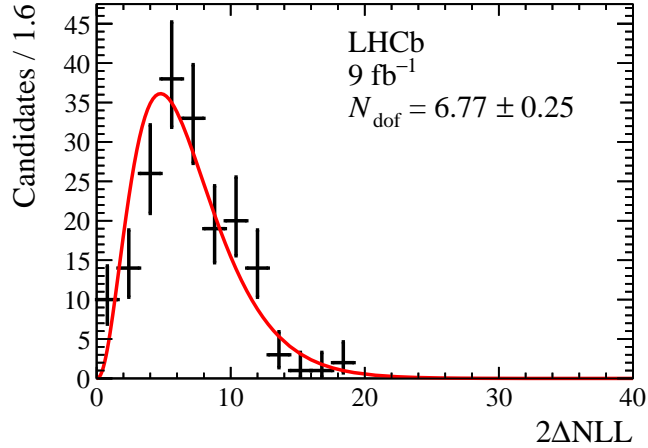


Figure 13: Distribution of $2\Delta\text{NLL}$ values used to estimate the significance of two $T_{c\bar{s}}$ contributions, where ΔNLL is the change in negative log likelihood between the fit results with model $f_0(500) + f_0(980)$ and model $f_0(500) + f_0(980) + \text{K-matrix } T_{c\bar{s}}$. The $2\Delta\text{NLL}$ distribution is fitted with a χ^2 distribution shown as red solid line.

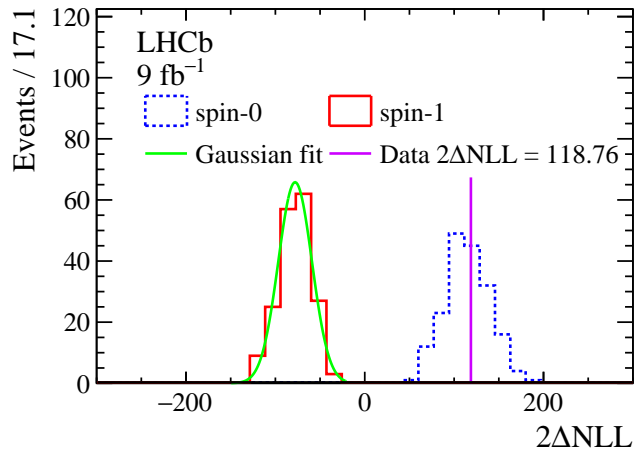


Figure 14: Distributions of $2\Delta\text{NLL}$ values used to estimate the significance of the $T_{c\bar{s}}$ spin-parity hypothesis, where ΔNLL is the change in negative log likelihood between the fit results with spin-1 and spin-0 hypotheses.

that $J^P = 0^+$ is favoured with high significance.

F Fit plots including interference contributions

The comparisons between data and fit results with different models including the interference contributions are shown in Figs. 15–17, where the interference contributions are mostly negative.

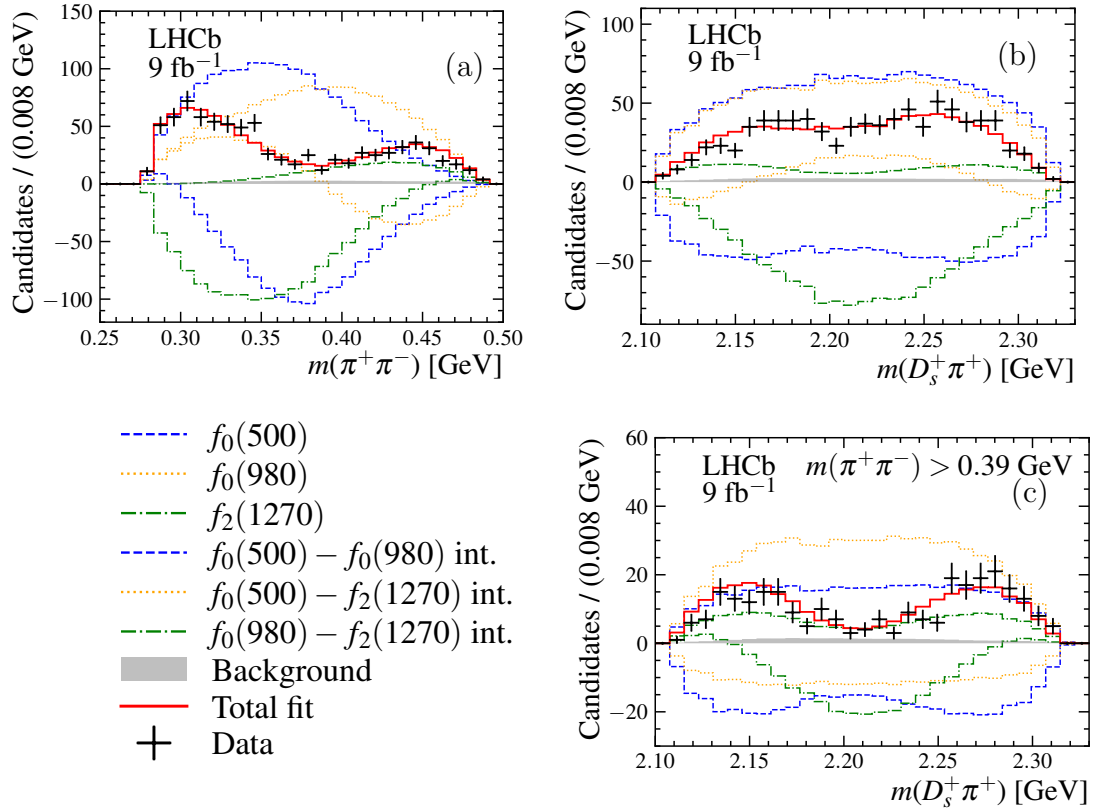


Figure 15: Comparison between data (black error bars) and results of the fit with the $f_0(500) + f_0(980) + f_2(1270)$ model (red solid line). The distributions are for the three channels combined in (a) $m(\pi^+\pi^-)$, (b) $m(D_s^+\pi^+)$, and (c) $m(D_s^+\pi^+)$ requiring $m(\pi^+\pi^-) > 0.39$ GeV. Individual components, corresponding to the background contribution estimated by $m(D_s^+\pi^+\pi^-)$ sideband regions (gray-filled) and different contributions from resonances (coloured dashed lines) and interference between the resonances (coloured dotted lines), are also shown as indicated in the legend.

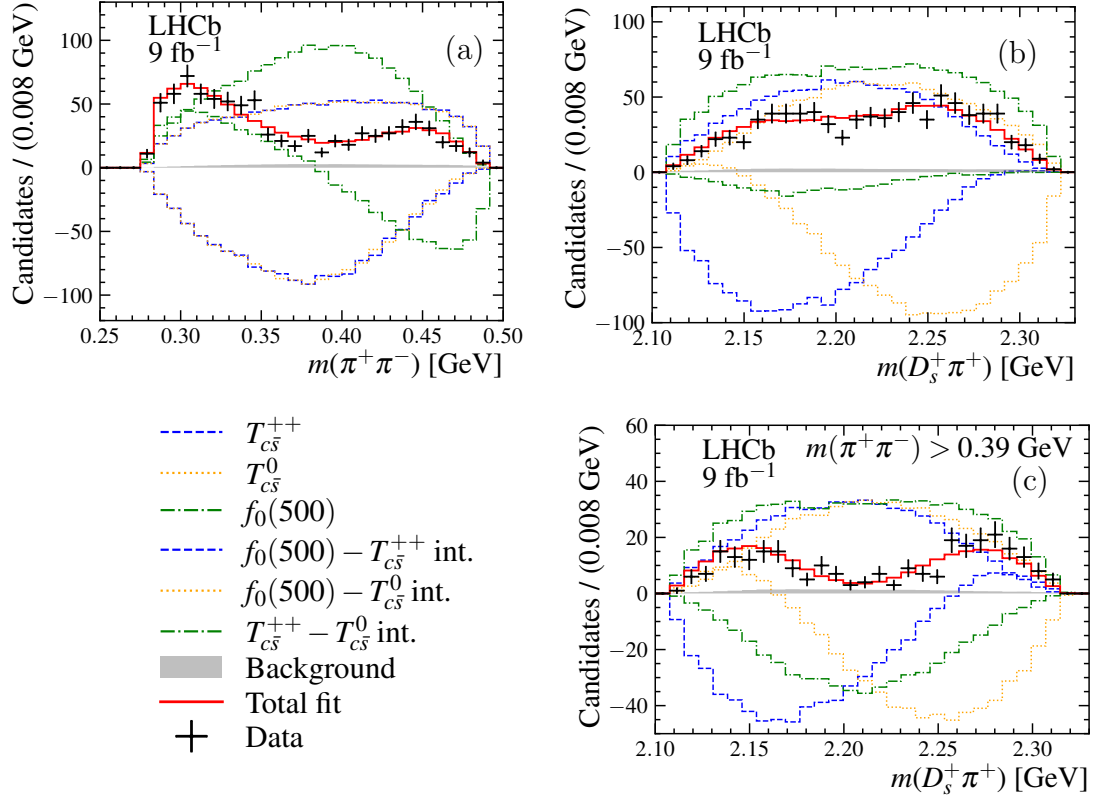


Figure 16: Comparison between data (black error bars) and results of the fit with the $f_0(500) +$ RBW $T_{c\bar{s}}(0^+)$ model (red solid line). The distributions are for the three channels combined in (a) $m(\pi^+\pi^-)$, (b) $m(D_s^+\pi^+)$, and (c) $m(D_s^+\pi^+)$ requiring $m(\pi^+\pi^-) > 0.39$ GeV. Individual components, corresponding to the background contribution estimated by $m(D_s^+\pi^+\pi^-)$ sideband regions (gray-filled) and different contributions from resonances (coloured dashed lines) and interference between the resonances (coloured dotted lines), are also shown as indicated in the legend.

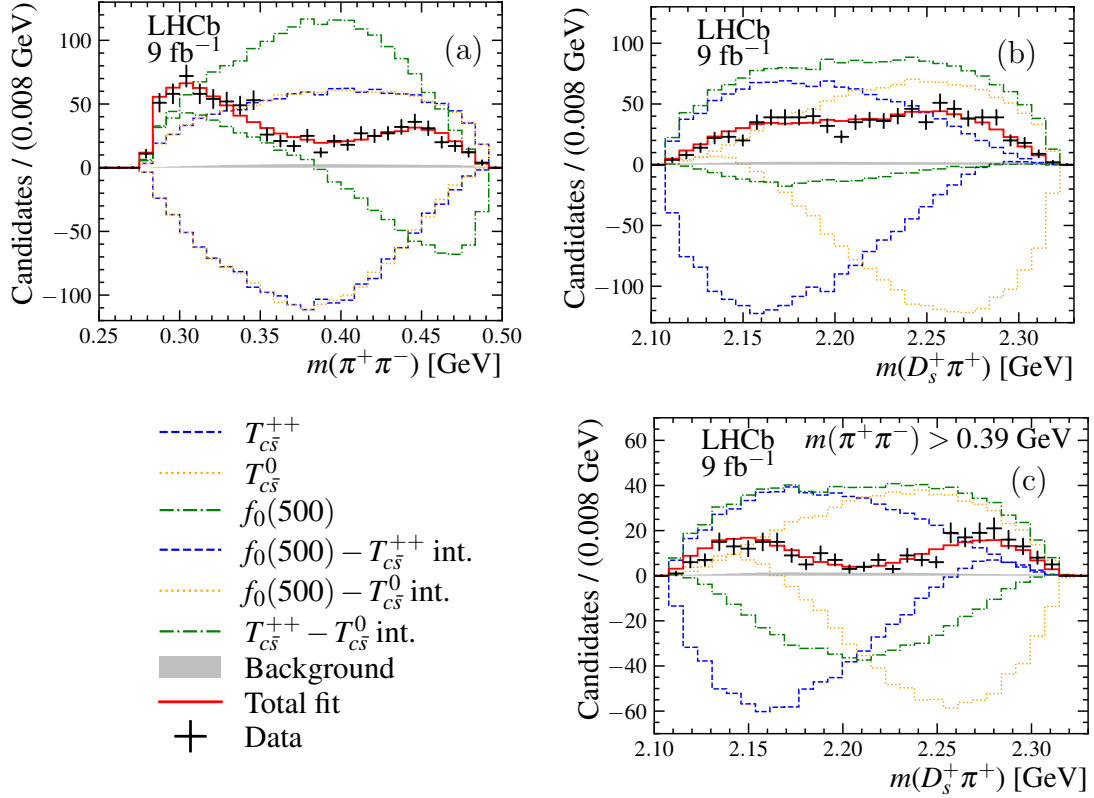


Figure 17: Comparison between data (black error bars) and results of the fit with the $f_0(500) +$ K-matrix $T_{c\bar{s}}(0^+)$ model (red solid line). The distributions are for the three channels combined in (a) $m(\pi^+\pi^-)$, (b) $m(D_s^+\pi^+)$, and (c) $m(D_s^+\pi^+)$ requiring $m(\pi^+\pi^-) > 0.39$ GeV. Individual components, corresponding to the background contribution estimated by $m(D_s^+\pi^+\pi^-)$ sideband regions (gray-filled) and different contributions from resonances (coloured dashed lines) and interference between the resonances (coloured dotted lines), are also shown as indicated in the legend.

References

- [1] BaBar collaboration, B. Aubert *et al.*, *Observation of a narrow meson decaying to $D_s^+\pi^0$ at a mass of $2.32\text{ GeV}/c^2$* , *Phys. Rev. Lett.* **90** (2003) 242001, [arXiv:hep-ex/0304021](#).
- [2] CLEO collaboration, D. Besson *et al.*, *Observation of a narrow resonance of mass $2.46\text{ GeV}/c^2$ decaying to $D_s^{*+}\pi^0$ and confirmation of the $D_{sJ}^*(2317)$ state*, *Phys. Rev.* **D68** (2003) 032002, Erratum *ibid.* **D75** (2007) 119908, [arXiv:hep-ex/0305100](#).
- [3] Y.-Q. Chen and X.-Q. Li, *A comprehensive four-quark interpretation of $D_s(2317)$, $D_s(2457)$ and $D_s(2632)$* , *Phys. Rev. Lett.* **93** (2004) 232001, [arXiv:hep-ph/0407062](#).
- [4] F.-K. Guo, P.-N. Shen, and H.-C. Chiang, *Dynamically generated 1^+ heavy mesons*, *Phys. Lett.* **B647** (2007) 133, [arXiv:hep-ph/0610008](#).
- [5] M. F. M. Lutz and M. Soyeur, *Radiative and isospin-violating decays of D_s -mesons in the hadrogenesis conjecture*, *Nucl. Phys.* **A813** (2008) 14, [arXiv:0710.1545](#).
- [6] J. L. Rosner, *Effects of S -wave thresholds*, *Phys. Rev.* **D74** (2006) 076006, [arXiv:hep-ph/0608102](#).
- [7] G. Q. Feng, X. H. Guo, and Z. H. Zhang, *Studying the D^*K molecular structure of $D_s(2460)$ in the Bethe-Salpeter approach*, *Eur. Phys. J.* **C72** (2012) 2033.
- [8] P. G. Ortega, J. Segovia, D. R. Entem, and F. Fernandez, *Molecular components in P -wave charmed-strange mesons*, *Phys. Rev.* **D94** (2016) 074037, [arXiv:1603.07000](#).
- [9] D. Zhang, Q.-Y. Zhao, and Q.-Y. Zhang, *A study of S -wave DK interactions in the chiral $SU(3)$ quark model*, *Chin. Phys. Lett.* **26** (2009) 091201, [arXiv:0905.1804](#).
- [10] T. Mehen and R. P. Springer, *Heavy-quark symmetry and the electromagnetic decays of excited charmed strange mesons*, *Phys. Rev.* **D70** (2004) 074014, [arXiv:hep-ph/0407181](#).
- [11] Belle collaboration, S.-K. Choi *et al.*, *Measurements of $B \rightarrow \bar{D}D_{s0}^{*+}(2317)$ decay rates and a search for isospin partners of the $D_{s0}^{*+}(2317)$* , *Phys. Rev.* **D91** (2015) 092011, Erratum *ibid.* **D92** (2015) 039905, [arXiv:1504.02637](#).
- [12] Hadron Spectrum collaboration, J. D. E. Yeo, C. E. Thomas, and D. J. Wilson, *$DK/D\pi$ scattering and an exotic virtual bound state at the $SU(3)$ flavour symmetric point from lattice QCD*, *JHEP* **07** (2024) 012, [arXiv:2403.10498](#).
- [13] S. Godfrey and N. Isgur, *Mesons in a relativized quark model with chromodynamics*, *Phys. Rev.* **D32** (1985) 189.
- [14] S. Godfrey and R. Kokoski, *Properties of P -wave mesons with one heavy quark*, *Phys. Rev.* **D43** (1991) 1679.
- [15] M. Di Pierro and E. Eichten, *Excited heavy-light systems and hadronic transitions*, *Phys. Rev.* **D64** (2001) 114004.

- [16] Particle Data Group, S. Navas *et al.*, *Review of particle physics*, *Phys. Rev.* **D110** (2024) 030001.
- [17] BaBar collaboration, B. Aubert *et al.*, *A study of the $D_{sJ}^*(2317)^+$ and $D_{sJ}(2460)^+$ mesons in inclusive $c\bar{c}$ production near $\sqrt{s} = 10.6$ GeV*, *Phys. Rev.* **D74** (2006) 032007, [arXiv:hep-ex/0604030](#).
- [18] Belle collaboration, Y. Mikami *et al.*, *Measurements of the D_{sJ} resonance properties*, *Phys. Rev. Lett.* **92** (2004) 012002, [arXiv:hep-ex/0307052](#).
- [19] M.-N. Tang *et al.*, *Isospin-conserving hadronic decay of the $D_{s1}(2460)$ into $D_s\pi^+\pi^-$* , *Commun. Theor. Phys.* **75** (2023) 055203, [arXiv:2303.18225](#).
- [20] LHCb collaboration, R. Aaij *et al.*, *Model-independent study of structure in $B^+ \rightarrow D^+D^-K^+$ decays*, *Phys. Rev. Lett.* **125** (2020) 242001, [arXiv:2009.00025](#).
- [21] LHCb collaboration, R. Aaij *et al.*, *Amplitude analysis of the $B^+ \rightarrow D^+D^-K^+$ decay*, *Phys. Rev.* **D102** (2020) 112003, [arXiv:2009.00026](#).
- [22] LHCb collaboration, R. Aaij *et al.*, *First observation of a doubly charged tetraquark candidate and its neutral partner*, *Phys. Rev. Lett.* **131** (2023) 041902, [arXiv:2212.02716](#).
- [23] LHCb collaboration, R. Aaij *et al.*, *Amplitude analysis of $B^0 \rightarrow \bar{D}^0D_s^+\pi^-$ and $B^+ \rightarrow D^-D_s^+\pi^+$ decays*, *Phys. Rev.* **D108** (2023) 012017, [arXiv:2212.02717](#).
- [24] H.-W. Ke, Y.-F. Shi, X.-H. Liu, and X.-Q. Li, *Possible molecular states of \bar{D}^*K^* (D^*K^*) and new exotic states $X_0(2900)$, $X_1(2900)$, $T_{cs0}^a(2900)^0$ and $T_{cs0}^a(2900)^{++}$* , *Phys. Rev.* **D106** (2022) 114032, [arXiv:2210.06215](#).
- [25] S. S. Agaev, K. Azizi, and H. Sundu, *Modeling the resonance $T_{cs0}^a(2900)^{++}$ as a hadronic molecule $D^{*+}K^{*+}$* , *Phys. Rev.* **D107** (2023) 094019, [arXiv:2212.12001](#).
- [26] M.-Y. Duan *et al.*, *Coupled-channel $D^*K^*-D_s^*\rho$ interactions and the origin of $T_{cs0}(2900)$* , *Phys. Rev.* **D108** (2023) 074006, [arXiv:2307.04092](#).
- [27] L. Maiani, A. D. Polosa, and V. Riquer, *Open charm tetraquarks in broken $SU(3)_F$ symmetry*, *Phys. Rev.* **D110** (2024) 034014, [arXiv:2405.08545](#).
- [28] K. Terasaki, *BABAR resonance as a new window of hadron physics*, *Phys. Rev.* **D68** (2003) 011501, [arXiv:hep-ph/0305213](#).
- [29] LHCb collaboration, A. A. Alves Jr. *et al.*, *The LHCb detector at the LHC*, *JINST* **3** (2008) S08005.
- [30] LHCb collaboration, R. Aaij *et al.*, *LHCb detector performance*, *Int. J. Mod. Phys.* **A30** (2015) 1530022, [arXiv:1412.6352](#).
- [31] T. Sjöstrand, S. Mrenna, and P. Skands, *A brief introduction to PYTHIA 8.1*, *Comput. Phys. Commun.* **178** (2008) 852, [arXiv:0710.3820](#); T. Sjöstrand, S. Mrenna, and P. Skands, *PYTHIA 6.4 physics and manual*, *JHEP* **05** (2006) 026, [arXiv:hep-ph/0603175](#).

- [32] I. Belyaev *et al.*, *Handling of the generation of primary events in Gauss, the LHCb simulation framework*, *J. Phys. Conf. Ser.* **331** (2011) 032047.
- [33] D. J. Lange, *The EvtGen particle decay simulation package*, *Nucl. Instrum. Meth.* **A462** (2001) 152.
- [34] N. Davidson, T. Przedzinski, and Z. Was, *PHOTOS interface in C++: Technical and physics documentation*, *Comp. Phys. Comm.* **199** (2016) 86, [arXiv:1011.0937](#).
- [35] Geant4 collaboration, J. Allison *et al.*, *Geant4 developments and applications*, *IEEE Trans. Nucl. Sci.* **53** (2006) 270; Geant4 collaboration, S. Agostinelli *et al.*, *Geant4: A simulation toolkit*, *Nucl. Instrum. Meth.* **A506** (2003) 250.
- [36] M. Clemencic *et al.*, *The LHCb simulation application, Gauss: Design, evolution and experience*, *J. Phys. Conf. Ser.* **331** (2011) 032023.
- [37] D. Müller, M. Clemencic, G. Corti, and M. Gersabeck, *ReDecay: A novel approach to speed up the simulation at LHCb*, *Eur. Phys. J.* **C78** (2018) 1009, [arXiv:1810.10362](#).
- [38] L. Breiman, J. H. Friedman, R. A. Olshen, and C. J. Stone, *Classification and regression trees*, [Wadsworth international group, Belmont, California, USA, 1984](#).
- [39] Y. Freund and R. E. Schapire, *A decision-theoretic generalization of on-line learning and an application to boosting*, *J. Comput. Syst. Sci.* **55** (1997) 119.
- [40] A. Höcker *et al.*, *TMVA - Toolkit for Multivariate Data Analysis*, [arXiv:physics/0703039](#); H. Voss, A. Höcker, J. Stelzer, and F. Tegenfeldt, *TMVA, the Toolkit for Multivariate Data Analysis with ROOT*, *PoS ACAT* (2009) 040.
- [41] W. D. Hulsbergen, *Decay chain fitting with a Kalman filter*, *Nucl. Instrum. Meth.* **A552** (2005) 566, [arXiv:physics/0503191](#).
- [42] ARGUS collaboration, H. Albrecht *et al.*, *Search for hadronic $b \rightarrow u$ decays*, *Phys. Lett.* **B241** (1990) 278.
- [43] G. N. Fleming, *Recoupling effects in the isobar model. I. General formalism for three-pion scattering*, *Phys. Rev.* **135** (1964) B551.
- [44] D. Morgan, *Phenomenological analysis of $I = \frac{1}{2}$ single-pion production processes in the energy range 500 to 700 MeV*, *Phys. Rev.* **166** (1968) 1731.
- [45] D. J. Herndon, P. Söding, and R. J. Cashmore, *Generalized isobar model formalism*, *Phys. Rev.* **D11** (1975) 3165.
- [46] S. M. Flatté, *Coupled-channel analysis of the $\pi\eta$ and $K\bar{K}$ systems near $K\bar{K}$ threshold*, *Phys. Lett.* **B63** (1976) 224.
- [47] D. V. Bugg, *Reanalysis of data on $a_0(1450)$ and $a_0(980)$* , *Phys. Rev.* **D78** (2008) 074023, [arXiv:0808.2706](#).
- [48] LHCb collaboration, R. Aaij *et al.*, *Measurement of resonant and CP components in $\bar{B}_s^0 \rightarrow J/\psi\pi^+\pi^-$ decays*, *Phys. Rev.* **D89** (2014) 092006, [arXiv:1402.6248](#).

- [49] I. J. R. Aitchison, *K-matrix formalism for overlapping resonances*, *Nucl. Phys.* **A189** (1972) 417.
- [50] V. V. Anisovich and A. V. Sarantsev, *K matrix analysis of the ($IJ^{PC} = 00^{++}$)-wave in the mass region below 1900 MeV*, *Eur. Phys. J.* **A16** (2003) 229, [arXiv:hep-ph/0204328](#).
- [51] JPAC collaboration, C. Fernández-Ramírez *et al.*, *Interpretation of the LHCb $P_c(4312)^+$ signal*, *Phys. Rev. Lett.* **123** (2019) 092001, [arXiv:1904.10021](#).
- [52] LHCb collaboration, R. Aaij *et al.*, *Measurement of the track reconstruction efficiency at LHCb*, *JINST* **10** (2015) P02007, [arXiv:1408.1251](#).
- [53] R. Aaij *et al.*, *The LHCb trigger and its performance in 2011*, *JINST* **8** (2013) P04022, [arXiv:1211.3055](#).
- [54] A. Poluektov, *Kernel density estimation of a multidimensional efficiency profile*, *JINST* **10** (2015) P02011, [arXiv:1411.5528](#).
- [55] LHCb collaboration, R. Aaij *et al.*, *Measurement of the resonant and CP components in $\bar{B}^0 \rightarrow J/\psi \pi^+ \pi^-$ decays*, *Phys. Rev.* **D90** (2014) 012003, [arXiv:1404.5673](#).
- [56] LHCb collaboration, R. Aaij *et al.*, *Dalitz plot analysis of $B^0 \rightarrow \bar{D}^0 \pi^+ \pi^-$ decays*, *Phys. Rev.* **D92** (2015) 032002, [arXiv:1505.01710](#).
- [57] LHCb collaboration, R. Aaij *et al.*, *Amplitude analysis of the $B^+ \rightarrow \pi^+ \pi^+ \pi^-$ decay*, *Phys. Rev.* **D101** (2020) 012006, [arXiv:1909.05211](#).
- [58] LHCb collaboration, R. Aaij *et al.*, *Amplitude analysis of the $D^+ \rightarrow \pi^- \pi^+ \pi^+$ decay and measurement of the $\pi^- \pi^+$ S-wave amplitude*, *JHEP* **06** (2023) 044, [arXiv:2208.03300](#).
- [59] LHCb collaboration, R. Aaij *et al.*, *Amplitude analysis of the $D_s^+ \rightarrow \pi^- \pi^+ \pi^+$ decay*, *JHEP* **07** (2023) 204, [arXiv:2209.09840](#).
- [60] BES collaboration, M. Ablikim *et al.*, *Resonances in $J/\psi \rightarrow \phi \pi^+ \pi^-$ and $\phi K^+ K^-$* , *Phys. Lett.* **B607** (2005) 243, [arXiv:hep-ex/0411001](#).
- [61] BESIII collaboration, M. Ablikim *et al.*, *Amplitude analysis of the decays $\eta' \rightarrow \pi^+ \pi^- \pi^0$ and $\eta' \rightarrow \pi^0 \pi^0 \pi^0$* , *Phys. Rev. Lett.* **118** (2017) 012001, [arXiv:1606.03847](#).
- [62] L. Liu *et al.*, *Interactions of charmed mesons with light pseudoscalar mesons from lattice QCD and implications on the nature of the $D_{s0}^*(2317)$* , *Phys. Rev.* **D87** (2013), [arXiv:1208.4535](#).
- [63] F.-K. Guo, C. Hanhart, and U.-G. Meissner, *Interactions between heavy mesons and Goldstone bosons from chiral dynamics*, *Eur. Phys. J.* **A40** (2009) 171, [arXiv:0901.1597](#).
- [64] T. Skwarnicki, *A study of the radiative cascade transitions between the Upsilon-prime and Upsilon resonances*, PhD thesis, Institute of Nuclear Physics, Krakow, 1986, [DESY-F31-86-02](#).

A. Padee⁴², K.O. Padeken¹⁸, B. Pagare⁵⁷, P.R. Pais²², T. Pajero⁴⁹, A. Palano²⁴,
M. Palutan²⁸, X. Pan^{4,b}, G. Panshin⁴⁴, L. Paolucci⁵⁷, A. Papanestis^{58,49},
M. Pappagallo^{24,g}, L.L. Pappalardo^{26,k}, C. Pappenheimer⁶⁶, C. Parkes⁶³, D.
Parmar⁷⁶, B. Passalacqua^{26,k}, G. Passaleva²⁷, D. Passaro^{35,q}, A. Pastore²⁴,
M. Patel⁶², J. Patoc⁶⁴, C. Patrignani^{25,i}, A. Paul⁶⁹, C.J. Pawley⁷⁹,
A. Pellegrino³⁸, J. Peng^{5,7}, M. Pepe Altarelli²⁸, S. Perazzini²⁵, D. Pereima⁴⁴, H.
Pereira Da Costa⁶⁸, A. Pereiro Castro⁴⁷, P. Perret¹¹, A. Perrevoort⁷⁸, A. Perro⁴⁹,
K. Petridis⁵⁵, A. Petrolini^{29,l}, J. P. Pfaller⁶⁶, H. Pham⁶⁹, L. Pica^{35,q},
M. Piccini³⁴, L. Piccolo³², B. Pietrzyk¹⁰, G. Pietrzyk¹⁴, D. Pinci³⁶, F. Pisani⁴⁹,
M. Pizzichemi^{31,n}, V. Placinta⁴³, M. Plo Casasus⁴⁷, T. Poeschl⁴⁹, F. Polci^{16,49},
M. Poli Lener²⁸, A. Poluektov¹³, N. Polukhina⁴⁴, I. Polyakov⁴⁴, E. Polycarpo³,
S. Ponce⁴⁹, D. Popov⁷, S. Poslavskii⁴⁴, K. Prasanth⁵⁹, C. Prouve⁸¹,
D. Provenzano^{32,j}, V. Pugatch⁵³, G. Punzi^{35,r}, S. Qasim⁵¹, Q. Q. Qian⁶,
W. Qian⁷, N. Qin^{4,b}, S. Qu^{4,b}, R. Quagliani⁴⁹, R.I. Rabadan Trejo⁵⁷,
J.H. Rademacker⁵⁵, M. Rama³⁵, M. Ramírez García⁸³, V. Ramos De Oliveira⁷⁰,
M. Ramos Pernas⁵⁷, M.S. Rangel³, F. Ratnikov⁴⁴, G. Raven³⁹,
M. Rebollo De Miguel⁴⁸, F. Redi^{30,h}, J. Reich⁵⁵, F. Reiss⁶³, Z. Ren⁷,
P.K. Resmi⁶⁴, R. Ribatti⁵⁰, G. R. Ricart^{15,12}, D. Riccardi^{35,q}, S. Ricciardi⁵⁸,
K. Richardson⁶⁵, M. Richardson-Slipper⁵⁹, K. Rinnert⁶¹, P. Robbe^{14,49},
G. Robertson⁶⁰, E. Rodrigues⁶¹, A. Rodriguez Alvarez⁴⁶, E. Rodriguez Fernandez⁴⁷,
J.A. Rodriguez Lopez⁷⁵, E. Rodriguez Rodriguez⁴⁷, J. Roensch¹⁹, A. Rogachev⁴⁴,
A. Rogovskiy⁵⁸, D.L. Rolf⁴⁹, P. Roloff⁴⁹, V. Romanovskiy⁶⁶, A. Romero Vidal⁴⁷,
G. Romolini²⁶, F. Ronchetti⁵⁰, T. Rong⁶, M. Rotondo²⁸, S. R. Roy²²,
M.S. Rudolph⁶⁹, M. Ruiz Diaz²², R.A. Ruiz Fernandez⁴⁷, J. Ruiz Vidal^{82,y},
A. Ryzhikov⁴⁴, J. Ryzka⁴⁰, J. J. Saavedra-Arias⁹, J.J. Saborido Silva⁴⁷, R. Sadek¹⁵,
N. Sagidova⁴⁴, D. Sahoo⁷⁷, N. Sahoo⁵⁴, B. Saitta^{32,j}, M. Salomoni^{31,n,49},
I. Sanderswood⁴⁸, R. Santacesaria³⁶, C. Santamarina Rios⁴⁷, M. Santimaria^{28,49},
L. Santoro², E. Santovetti³⁷, A. Saputi^{26,49}, D. Saranin⁴⁴, A. Sarnatskiy⁷⁸,
G. Sarpis⁵⁹, M. Sarpis⁶³, C. Satriano^{36,s}, A. Satta³⁷, M. Saur⁶, D. Savrina⁴⁴,
H. Sazak¹⁷, L.G. Scantlebury Smead⁶⁴, A. Scarabotto¹⁹, S. Schael¹⁷, S. Scherl⁶¹,
M. Schiller⁶⁰, H. Schindler⁴⁹, M. Schmelling²¹, B. Schmidt⁴⁹, S. Schmitt¹⁷,
H. Schmitz¹⁸, O. Schneider⁵⁰, A. Schopper⁴⁹, N. Schulte¹⁹, S. Schulte⁵⁰,
M.H. Schune¹⁴, R. Schwemmer⁴⁹, G. Schwering¹⁷, B. Sciascia²⁸, A. Sciucchi⁴⁹,
S. Sellam⁴⁷, A. Semennikov⁴⁴, T. Senger⁵¹, M. Senghi Soares³⁹, A. Sergi²⁹,
N. Serra⁵¹, L. Sestini³³, A. Seuthe¹⁹, Y. Shang⁶, D.M. Shangase⁸³, M. Shapkin⁴⁴,
R. S. Sharma⁶⁹, I. Shchemerov⁴⁴, L. Shchutska⁵⁰, T. Shears⁶¹, L. Shekhtman⁴⁴,
Z. Shen⁶, S. Sheng^{5,7}, V. Shevchenko⁴⁴, B. Shi⁷, Q. Shi⁷, Y. Shimizu¹⁴,
E. Shmanin²⁵, R. Shorkin⁴⁴, J.D. Shupperd⁶⁹, R. Silva Coutinho⁶⁹, G. Simi^{33,o},
S. Simone^{24,g}, N. Skidmore⁵⁷, T. Skwarnicki⁶⁹, M.W. Slater⁵⁴, J.C. Smallwood⁶⁴,
E. Smith⁶⁵, K. Smith⁶⁸, M. Smith⁶², A. Snoch³⁸, L. Soares Lavra⁵⁹,
M.D. Sokoloff⁶⁶, F.J.P. Soler⁶⁰, A. Solomin^{44,55}, A. Solovev⁴⁴, I. Solovyev⁴⁴, N. S.
Sommerfeld¹⁸, R. Song¹, Y. Song⁵⁰, Y. Song^{4,b}, Y. S. Song⁶,
F.L. Souza De Almeida⁶⁹, B. Souza De Paula³, E. Spadaro Norella²⁹, E. Spedicato²⁵,
J.G. Speer¹⁹, E. Spiridenkov⁴⁴, P. Spradlin⁶⁰, V. Sriskaran⁴⁹, F. Stagni⁴⁹,
M. Stahl⁴⁹, S. Stahl⁴⁹, S. Stanislaus⁶⁴, E.N. Stein⁴⁹, O. Steinkamp⁵¹,
O. Stenyakin⁴⁴, H. Stevens¹⁹, D. Strelakina⁴⁴, Y. Su⁷, F. Suljik⁶⁴, J. Sun³²,
L. Sun⁷⁴, D. Sundfeld², W. Sutcliffe⁵¹, P.N. Swallow⁵⁴, K. Swientek⁴⁰,
F. Swystun⁵⁶, A. Szabelski⁴², T. Szumlak⁴⁰, Y. Tan^{4,b}, Y. Tang⁷⁴, M.D. Tat⁶⁴,
A. Terentev⁴⁴, F. Terzuoli^{35,u,49}, F. Teubert⁴⁹, E. Thomas⁴⁹, D.J.D. Thompson⁵⁴,
H. Tilquin⁶², V. Tisserand¹¹, S. T'Jampens¹⁰, M. Tobin^{5,49}, L. Tomassetti^{26,k},

G. Tonani^{30,m,49} , X. Tong⁶ , D. Torres Machado² , L. Toscano¹⁹ , D.Y. Tou^{4,b} ,
C. Tripp¹⁴⁵ , G. Tuci²² , N. Tuning³⁸ , L.H. Uecker²² , A. Ukleja⁴⁰ ,
D.J. Unverzagt²² , B. Urbach⁵⁹ , E. Ursov⁴⁴ , A. Usachov³⁹ , A. Ustyuzhanin⁴⁴ ,
U. Uwer²² , V. Vagnoni²⁵ , V. Valcarce Cadenas⁴⁷ , G. Valenti²⁵ ,
N. Valls Canudas⁴⁹ , H. Van Hecke⁶⁸ , E. van Herwijnen⁶² , C.B. Van Hulse^{47,w} ,
R. Van Laak⁵⁰ , M. van Veghel³⁸ , G. Vasquez⁵¹ , R. Vazquez Gomez⁴⁶ ,
P. Vazquez Regueiro⁴⁷ , C. Vázquez Sierra⁴⁷ , S. Vecchi²⁶ , J.J. Velthuis⁵⁵ ,
M. Veltri^{27,v} , A. Venkateswaran⁵⁰ , M. Verdoglia³² , M. Vesterinen⁵⁷ , D.
Vico Benet⁶⁴ , P. V. Vidrier Villalba⁴⁶ , M. Vieites Diaz⁴⁹ , X. Vilasis-Cardona⁴⁵ ,
E. Vilella Figueras⁶¹ , A. Villa²⁵ , P. Vincent¹⁶ , F.C. Volle⁵⁴ , D. vom Bruch¹³ ,
N. Voropaev⁴⁴ , K. Vos⁷⁹ , C. Vrahas⁵⁹ , J. Wagner¹⁹ , J. Walsh³⁵ , E.J. Walton^{1,57} ,
G. Wan⁶ , C. Wang²² , G. Wang⁸ , J. Wang⁶ , J. Wang⁵ , J. Wang^{4,b} , J. Wang⁷⁴ ,
M. Wang³⁰ , N. W. Wang⁷ , R. Wang⁵⁵ , X. Wang⁸ , X. Wang⁷² , X. W. Wang⁶² ,
Y. Wang⁶ , Z. Wang¹⁴ , Z. Wang^{4,b} , Z. Wang³⁰ , J.A. Ward^{57,1} , M. Waterlaet⁴⁹ ,
N.K. Watson⁵⁴ , D. Websdale⁶² , Y. Wei⁶ , J. Wendel⁸¹ , B.D.C. Westhenry⁵⁵ ,
C. White⁵⁶ , M. Whitehead⁶⁰ , E. Whiter⁵⁴ , A.R. Wiederhold⁶³ , D. Wiedner¹⁹ ,
G. Wilkinson⁶⁴ , M.K. Wilkinson⁶⁶ , M. Williams⁶⁵ , M. J. Williams⁴⁹ ,
M.R.J. Williams⁵⁹ , R. Williams⁵⁶ , Z. Williams⁵⁵ , F.F. Wilson⁵⁸ , M. Winn¹² ,
W. Wislicki⁴² , M. Witek⁴¹ , L. Witola²² , G. Wormser¹⁴ , S.A. Wotton⁵⁶ , H. Wu⁶⁹ ,
J. Wu⁸ , X. Wu⁷⁴ , Y. Wu⁶ , Z. Wu⁷ , K. Wyllie⁴⁹ , S. Xian⁷² , Z. Xiang⁵ , Y. Xie⁸ ,
A. Xu³⁵ , J. Xu⁷ , L. Xu^{4,b} , L. Xu^{4,b} , M. Xu⁵⁷ , Z. Xu⁴⁹ , Z. Xu⁷ , Z. Xu⁵ , K.
Yang⁶² , S. Yang⁷ , X. Yang⁶ , Y. Yang^{29,l} , Z. Yang⁶ , V. Yeroshenko¹⁴ ,
H. Yeung⁶³ , H. Yin⁸ , C. Y. Yu⁶ , J. Yu⁷¹ , X. Yuan⁵ , Y. Yuan^{5,7} ,
E. Zaffaroni⁵⁰ , M. Zavertyaev²¹ , M. Zdybal⁴¹ , F. Zenesini^{25,i} , C. Zeng^{5,7} ,
M. Zeng^{4,b} , C. Zhang⁶ , D. Zhang⁸ , J. Zhang⁷ , L. Zhang^{4,b} , S. Zhang⁷¹ ,
S. Zhang⁶⁴ , Y. Zhang⁶ , Y. Z. Zhang^{4,b} , Y. Zhao²² , A. Zharkova⁴⁴ ,
A. Zhelezov²² , S. Z. Zheng⁶ , X. Z. Zheng^{4,b} , Y. Zheng⁷ , T. Zhou⁶ , X. Zhou⁸ ,
Y. Zhou⁷ , V. Zhovkovska⁵⁷ , L. Z. Zhu⁷ , X. Zhu^{4,b} , X. Zhu⁸ , V. Zhukov¹⁷ ,
J. Zhuo⁴⁸ , Q. Zou^{5,7} , D. Zuliani^{33,o} , G. Zunica⁵⁰ .

¹*School of Physics and Astronomy, Monash University, Melbourne, Australia*

²*Centro Brasileiro de Pesquisas Físicas (CBPF), Rio de Janeiro, Brazil*

³*Universidade Federal do Rio de Janeiro (UFRJ), Rio de Janeiro, Brazil*

⁴*Department of Engineering Physics, Tsinghua University, Beijing, China, Beijing, China*

⁵*Institute Of High Energy Physics (IHEP), Beijing, China*

⁶*School of Physics State Key Laboratory of Nuclear Physics and Technology, Peking University, Beijing, China*

⁷*University of Chinese Academy of Sciences, Beijing, China*

⁸*Institute of Particle Physics, Central China Normal University, Wuhan, Hubei, China*

⁹*Consejo Nacional de Rectores (CONARE), San Jose, Costa Rica*

¹⁰*Université Savoie Mont Blanc, CNRS, IN2P3-LAPP, Annecy, France*

¹¹*Université Clermont Auvergne, CNRS/IN2P3, LPC, Clermont-Ferrand, France*

¹²*Departement de Physique Nucleaire (SPhN), Gif-Sur-Yvette, France*

¹³*Aix Marseille Univ, CNRS/IN2P3, CPPM, Marseille, France*

¹⁴*Université Paris-Saclay, CNRS/IN2P3, IJCLab, Orsay, France*

¹⁵*Laboratoire Leprince-Ringuet, CNRS/IN2P3, Ecole Polytechnique, Institut Polytechnique de Paris, Palaiseau, France*

¹⁶*LPNHE, Sorbonne Université, Paris Diderot Sorbonne Paris Cité, CNRS/IN2P3, Paris, France*

¹⁷*I. Physikalisches Institut, RWTH Aachen University, Aachen, Germany*

¹⁸*Universität Bonn - Helmholtz-Institut für Strahlen und Kernphysik, Bonn, Germany*

¹⁹*Fakultät Physik, Technische Universität Dortmund, Dortmund, Germany*

²⁰*Physikalisches Institut, Albert-Ludwigs-Universität Freiburg, Freiburg, Germany*

²¹*Max-Planck-Institut für Kernphysik (MPIK), Heidelberg, Germany*

- ²² *Physikalisches Institut, Ruprecht-Karls-Universität Heidelberg, Heidelberg, Germany*
- ²³ *School of Physics, University College Dublin, Dublin, Ireland*
- ²⁴ *INFN Sezione di Bari, Bari, Italy*
- ²⁵ *INFN Sezione di Bologna, Bologna, Italy*
- ²⁶ *INFN Sezione di Ferrara, Ferrara, Italy*
- ²⁷ *INFN Sezione di Firenze, Firenze, Italy*
- ²⁸ *INFN Laboratori Nazionali di Frascati, Frascati, Italy*
- ²⁹ *INFN Sezione di Genova, Genova, Italy*
- ³⁰ *INFN Sezione di Milano, Milano, Italy*
- ³¹ *INFN Sezione di Milano-Bicocca, Milano, Italy*
- ³² *INFN Sezione di Cagliari, Monserrato, Italy*
- ³³ *INFN Sezione di Padova, Padova, Italy*
- ³⁴ *INFN Sezione di Perugia, Perugia, Italy*
- ³⁵ *INFN Sezione di Pisa, Pisa, Italy*
- ³⁶ *INFN Sezione di Roma La Sapienza, Roma, Italy*
- ³⁷ *INFN Sezione di Roma Tor Vergata, Roma, Italy*
- ³⁸ *Nikhef National Institute for Subatomic Physics, Amsterdam, Netherlands*
- ³⁹ *Nikhef National Institute for Subatomic Physics and VU University Amsterdam, Amsterdam, Netherlands*
- ⁴⁰ *AGH - University of Krakow, Faculty of Physics and Applied Computer Science, Kraków, Poland*
- ⁴¹ *Henryk Niewodniczanski Institute of Nuclear Physics Polish Academy of Sciences, Kraków, Poland*
- ⁴² *National Center for Nuclear Research (NCBJ), Warsaw, Poland*
- ⁴³ *Horia Hulubei National Institute of Physics and Nuclear Engineering, Bucharest-Magurele, Romania*
- ⁴⁴ *Affiliated with an institute covered by a cooperation agreement with CERN*
- ⁴⁵ *DS4DS, La Salle, Universitat Ramon Llull, Barcelona, Spain*
- ⁴⁶ *ICCUB, Universitat de Barcelona, Barcelona, Spain*
- ⁴⁷ *Instituto Galego de Física de Altas Enerxías (IGFAE), Universidade de Santiago de Compostela, Santiago de Compostela, Spain*
- ⁴⁸ *Instituto de Física Corpuscular, Centro Mixto Universidad de Valencia - CSIC, Valencia, Spain*
- ⁴⁹ *European Organization for Nuclear Research (CERN), Geneva, Switzerland*
- ⁵⁰ *Institute of Physics, Ecole Polytechnique Fédérale de Lausanne (EPFL), Lausanne, Switzerland*
- ⁵¹ *Physik-Institut, Universität Zürich, Zürich, Switzerland*
- ⁵² *NSC Kharkiv Institute of Physics and Technology (NSC KIPT), Kharkiv, Ukraine*
- ⁵³ *Institute for Nuclear Research of the National Academy of Sciences (KINR), Kyiv, Ukraine*
- ⁵⁴ *School of Physics and Astronomy, University of Birmingham, Birmingham, United Kingdom*
- ⁵⁵ *H.H. Wills Physics Laboratory, University of Bristol, Bristol, United Kingdom*
- ⁵⁶ *Cavendish Laboratory, University of Cambridge, Cambridge, United Kingdom*
- ⁵⁷ *Department of Physics, University of Warwick, Coventry, United Kingdom*
- ⁵⁸ *STFC Rutherford Appleton Laboratory, Didcot, United Kingdom*
- ⁵⁹ *School of Physics and Astronomy, University of Edinburgh, Edinburgh, United Kingdom*
- ⁶⁰ *School of Physics and Astronomy, University of Glasgow, Glasgow, United Kingdom*
- ⁶¹ *Oliver Lodge Laboratory, University of Liverpool, Liverpool, United Kingdom*
- ⁶² *Imperial College London, London, United Kingdom*
- ⁶³ *Department of Physics and Astronomy, University of Manchester, Manchester, United Kingdom*
- ⁶⁴ *Department of Physics, University of Oxford, Oxford, United Kingdom*
- ⁶⁵ *Massachusetts Institute of Technology, Cambridge, MA, United States*
- ⁶⁶ *University of Cincinnati, Cincinnati, OH, United States*
- ⁶⁷ *University of Maryland, College Park, MD, United States*
- ⁶⁸ *Los Alamos National Laboratory (LANL), Los Alamos, NM, United States*
- ⁶⁹ *Syracuse University, Syracuse, NY, United States*
- ⁷⁰ *Pontifícia Universidade Católica do Rio de Janeiro (PUC-Rio), Rio de Janeiro, Brazil, associated to ³*
- ⁷¹ *School of Physics and Electronics, Hunan University, Changsha City, China, associated to ⁸*
- ⁷² *Guangdong Provincial Key Laboratory of Nuclear Science, Guangdong-Hong Kong Joint Laboratory of Quantum Matter, Institute of Quantum Matter, South China Normal University, Guangzhou, China, associated to*
- ⁷³ *Lanzhou University, Lanzhou, China, associated to ⁵*

- ⁷⁴ *School of Physics and Technology, Wuhan University, Wuhan, China, associated to*
⁷⁵ *Departamento de Física , Universidad Nacional de Colombia, Bogota, Colombia, associated to* ¹⁶
⁷⁶ *Ruhr Universitaet Bochum, Fakultaet f. Physik und Astronomie, Bochum, Germany, associated to* ¹⁹
⁷⁷ *Eotvos Lorand University, Budapest, Hungary, associated to* ⁴⁹
⁷⁸ *Van Swinderen Institute, University of Groningen, Groningen, Netherlands, associated to* ³⁸
⁷⁹ *Universiteit Maastricht, Maastricht, Netherlands, associated to* ³⁸
⁸⁰ *Tadeusz Kosciuszko Cracow University of Technology, Cracow, Poland, associated to* ⁴¹
⁸¹ *Universidad de Coruña, A Coruna, Spain, associated to* ⁴⁵
⁸² *Department of Physics and Astronomy, Uppsala University, Uppsala, Sweden, associated to* ⁶⁰
⁸³ *University of Michigan, Ann Arbor, MI, United States, associated to* ⁶⁹

^a *Centro Federal de Educaco Tecnolgica Celso Suckow da Fonseca, Rio De Janeiro, Brazil*

^b *Center for High Energy Physics, Tsinghua University, Beijing, China*

^c *Hangzhou Institute for Advanced Study, UCAS, Hangzhou, China*

^d *School of Physics and Electronics, Henan University , Kaifeng, China*

^e *LIP6, Sorbonne Universit, Paris, France*

^f *Universidad Nacional Autnoma de Honduras, Tegucigalpa, Honduras*

^g *Universit di Bari, Bari, Italy*

^h *Universit di Bergamo, Bergamo, Italy*

ⁱ *Universit di Bologna, Bologna, Italy*

^j *Universit di Cagliari, Cagliari, Italy*

^k *Universit di Ferrara, Ferrara, Italy*

^l *Universit di Genova, Genova, Italy*

^m *Universit degli Studi di Milano, Milano, Italy*

ⁿ *Universit degli Studi di Milano-Bicocca, Milano, Italy*

^o *Universit di Padova, Padova, Italy*

^p *Universit di Perugia, Perugia, Italy*

^q *Scuola Normale Superiore, Pisa, Italy*

^r *Universit di Pisa, Pisa, Italy*

^s *Universit della Basilicata, Potenza, Italy*

^t *Universit di Roma Tor Vergata, Roma, Italy*

^u *Universit di Siena, Siena, Italy*

^v *Universit di Urbino, Urbino, Italy*

^w *Universidad de Alcal, Alcal de Henares , Spain*

^x *Facultad de Ciencias Fsicas, Madrid, Spain*

^y *Department of Physics/Division of Particle Physics, Lund, Sweden*

[†] *Deceased*